Cell morphology drives spatial patterning in microbial communities

William P. J. Smith[a], Yohan Davit[b], James M. Osborne[c], Wook Kim[d,1], Kevin R. Foster[d,2], and Joe M. Pitt-Francis[a,2]

[a]Department of Computer Science, University of Oxford, Oxford OX1 3QD, United Kingdom; [b]Institut de Mécanique des Fluides de Toulouse (IMFT), Université de Toulouse, Centre National de la Recherche Scientifique (CNRS), Institut National Polytechnique de Toulouse (INPT), Université Paul Sabatier (UPS), F-31400 Toulouse, France; [c]School of Mathematics and Statistics, University of Melbourne, VIC 3010, Australia; and [d]Department of Zoology, University of Oxford, Oxford OX1 3PS, United Kingdom

The clearest phenotypic characteristic of microbial cells is their shape, but we do not understand how cell shape affects the dense communities, known as biofilms, where many microbes live. Here, we use individual-based modeling to systematically vary cell shape and study its impact in simulated communities. We compete cells with different cell morphologies under a range of conditions and ask how shape affects the patterning and evolutionary fitness of cells within a community. Our models predict that cell shape will strongly influence the fate of a cell lineage: we describe a mechanism through which coccal (round) cells rise to the upper surface of a community, leading to a strong spatial structuring that can be critical for fitness. We test our predictions experimentally using strains of *Escherichia coli* that grow at a similar rate but differ in cell shape due to single amino acid changes in the actin homolog MreB. As predicted by our model, cell types strongly sort by shape, with round cells at the top of the colony and rod cells dominating the basal surface and edges. Our work suggests that cell morphology has a strong impact within microbial communities and may offer new ways to engineer the structure of synthetic communities.

biofilms | cell morphology | biophysics | self-organization | synthetic biology

Single-celled microorganisms such as bacteria display significant morphological diversity, ranging from the simple to the complex and exotic (1–3). Phylogenetic studies indicate that particular morphologies have evolved independently multiple times, suggesting that the myriad shapes of modern bacteria may be adaptations to particular environments (4–6). Microbes can also actively change their morphology in response to environmental stimuli, such as changes to nutrient levels or predation (7, 8). However, understanding when and why particular cell shapes offer a competitive edge remains an unresolved question in microbiology.

Previous studies have characterized selective pressures favoring particular shapes (7, 9–11): for example, highly viscous environments may select for the helical cell morphologies observed in spirochete bacteria (12). Thus far, these studies have predominantly focused on selective pressures acting at the level of the individual cell. However, many species live in dense, surface-associated communities known as biofilms, which are fundamental to the biology of microbes and how they affect us—playing major roles in the human microbiome, chronic diseases, antibiotic resistance, biofouling, and waste-water treatment (13–17). As a result, there has been an intensive effort in recent years to understand how the biofilm mode of growth affects microbes and their evolution (18, 19), but we know very little of the importance of cell shape for biofilm biology.

In biofilms, microbial cells are often in close physical contact, making mechanical interactions between neighboring cells particularly significant. Recent studies have suggested that rod-shaped cells can drive collective behaviors in microbial groups because of their tendency to align their orientations with nearby

cells and surfaces (20, 21). The resulting orientational order affects how cell groups expand in microfluidic channels and enables motile cells to swarm together in raft-like collectives (22, 23). Aligned cells are also subject to buckling interactions, which fold neighboring cell groups into one another to form fractal-like interdigitations (21, 24), and differences in cell sizes may drive depletion effects that lead to genetic demixing (25). These studies suggest that, by influencing biomechanical interactions between microbes, shape may have far-reaching consequences for the properties and prospects of a cell within a community.

Individual-based modeling has emerged as a powerful way to study biofilms. These models serve as a testing ground to study how phenotypes, including adhesion, antibiotics, and extracellular polymeric substances (EPSs), affect individual strains and biofilms as a whole (26–31). However, the majority of individual-based models do not allow cell shape to be altered (32). We have therefore developed a flexible simulation framework that allows us to incorporate cell shape alongside cell division, physical interactions, and metabolic interactions via nutrient consumption. Our analyses identify a mechanism by which different cell shapes can self-organize into layered structures, thereby providing particular genotypes with preferential access to favorable positions in the biofilm. We test our model predictions with experiments in which mutant *Escherichia coli* strains of different shapes are

Significance

Microbial communities contain cells of different shapes, and yet we know little about how these shapes affect community biology. We have developed a computational model to study the effects of microbial shape in communities. Our model predicts that shape will have strong effects on cells' positioning, and, consequently, their survival and reproduction. Rod-shaped cells are better at colonizing the base of the community and its expanding edges, whereas round cells dominate the upper surface. We show that the same patterns occur in colonies of *Escherichia coli*, using strains with different shapes. Our work suggests that cell shape is a major determinant of patterning and evolutionary fitness within microbial communities.

cultured together in colonies. Our work shows that differences in cell shape are central to both spatial architecture and fitness within microbial communities.

Results

To explore the consequences of bacterial cell shape within the biofilm environment, we used two approaches: computer simulations with an individual-based hybrid model (IbM) framework and experiments in which differently shaped bacteria are cultured together on agar plates.

Here, we introduce the model and its predictions, before going on to describe the experiments that we subsequently devised and performed to test it.

Individual-Based Modeling. Our IbM framework considers microbial communities as collections of elongating cells on a hard surface (Fig. 1, times t1 and t2). Cells absorb diffusing nutrients from their surroundings to grow and divide, causing the community to expand in space (Fig. 1, "Dynamics"). All cells are represented as capsules of segment length l and radius r (Fig. 1, *Top*); bacillar and coccal cell shapes are modeled using short (S) or long (L) capsules, whose geometries approximate those of *Staphylococcus aureus* and *E. coli*, respectively (Fig. 1, "Cells") (24, 33). Although simple, these morphologies are ubiquitous and frequently found together in bacterial communities (4, 7).

Overall, our model is similar in structure to previous models based on spherical cells (26–28), except that we can now also study communities containing nonspherical cell shapes. Although this extension requires the underlying mathematical formulation to be more detailed, our model is conceptually only incrementally more complex and, therefore, an appropriate minimum model for investigating the influences of cell shape in
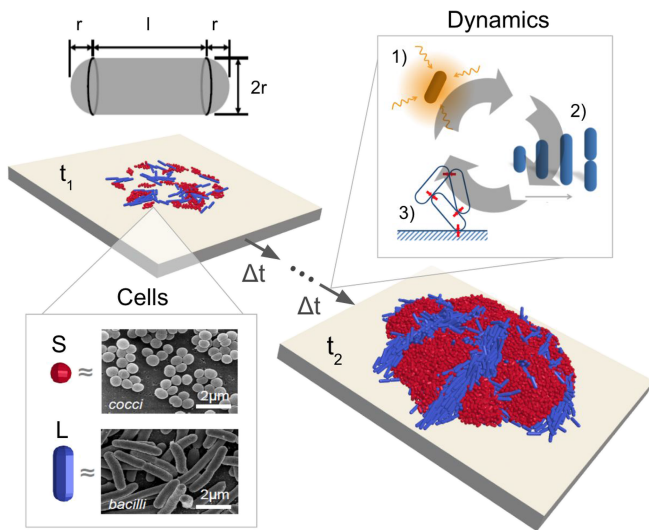
Fig. 1. To simulate the growth of a mixed-species bacterial colony on a hard surface, we use a mixed-morphotype hybrid model. Bacterial cells are represented using rigid elastic capsules of variable length *l* and fixed radius *r* (*Top Left*); coccal and bacillar cells are approximated respectively using long (L) and short (S) capsules ("Cells"). Micrographs depict *S. aureus* (*Top*) and *Escherichia coli* (*Bottom*) bacteria. Biofilm growth is driven by three primary processes ("Dynamics"): cells absorb nutrients from their surroundings (process 1) to grow and divide (process 2), and repulsive interactions between growing cells lead to the expansion of the colony in three dimensions (process 3). By sequentially updating the cell configuration according to these rules, we simulate the development of colony structure from an initial inoculum of cells (time t1) to a mature biofilm (time t2). Micrographs provided by the Public Health Image Library (34) and Rocky Mountain Laboratories (35).
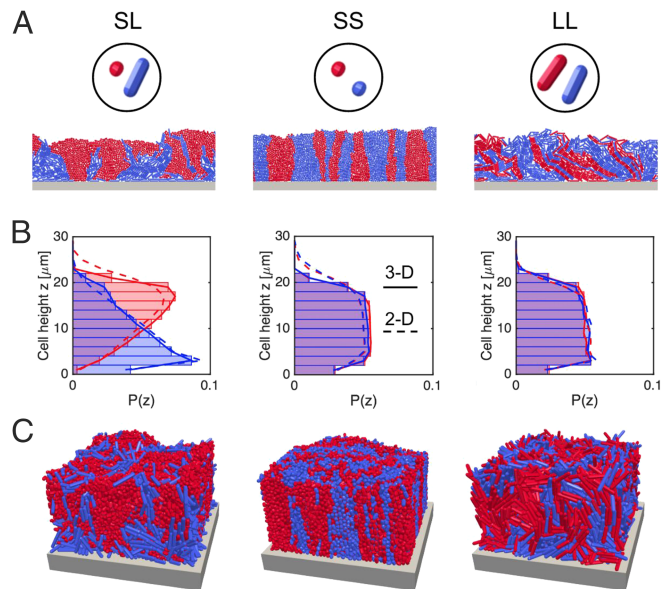

Fig. 2. Cell morphology affects self-organization in simulations of exponential biofilm growth. (*A*) Sections of 2D biofilms grown from 1:1 mixtures of red- and blue-labeled strains form different spatial patterns depending on whether the strains have a coccal (short, S) or rod-like (long, L) morphology. (*B*) Volume-weighted histograms of cell *z* coordinates (*P(z)*) show that SL mixtures develop a layered structure in both 2D and 3D colonies, with S cells sitting above L cells. In SS and LL control simulations, this layering is absent. (*C*) Three-dimensional simulations, in which cell positions and orientations are no longer confined to the *xz* plane, produce spatial patterns similar to those shown in 2D. There were 20 simulations per case.

microbial communities. Further details on the framework are provided in *SI Appendix*.

Cell Shape Drives Spatial Patterning Within Colonies. We first used our model framework to simulate the growth of vertical biofilm sections in two and three dimensions. In the 2D simulations, we used very thin domains so that cells were forced to grow as a monolayer; 3D simulations lift this constraint and allow full freedom of movement. Initial conditions and domain boundary treatments are described in *Materials and Methods*. As a first approximation, we allowed all cells to grow exponentially at a maximal growth rate μ_{max}, representing a scenario where nutrient perfusion in the biofilm is complete and spatially homogeneous. Later in this study, we remove this assumption to model competitive interactions between different cell shapes.

To investigate the impact of cell shape on biofilm growth, we grew colonies using three 1:1 combinations of S and L cell shapes, as shown at the top of Fig. 2 (SL, SS, and LL mixtures). We found that different spatial structures emerged, depending on the cell shapes that were present. SL cell mixtures spontaneously developed a layered structure, with groups of red S cells lying atop blue L cells. By contrast, SS mixtures tended to produce smooth, vertical boundaries between adjacent strain groups, with no layering. LL colonies produced a third type of spatial patterning, developing fractal-like interdigitations between adjacent cell groups, as reported in previous modeling studies (24, 32).

For these three cases, representative end-state snapshots of 2D colonies are shown in Fig. 2*A*, whereas Movie S1 shows these colonies growing side-by-side. In Fig. 2*B*, we plot histograms of cell *z* coordinates for the two strains: here, $P(z)$ corresponds to the biovolume distribution along the *z* axis, normalized by total colony volume. This distribution quantifies the tendency for SL colonies to develop layered structures; by contrast, the
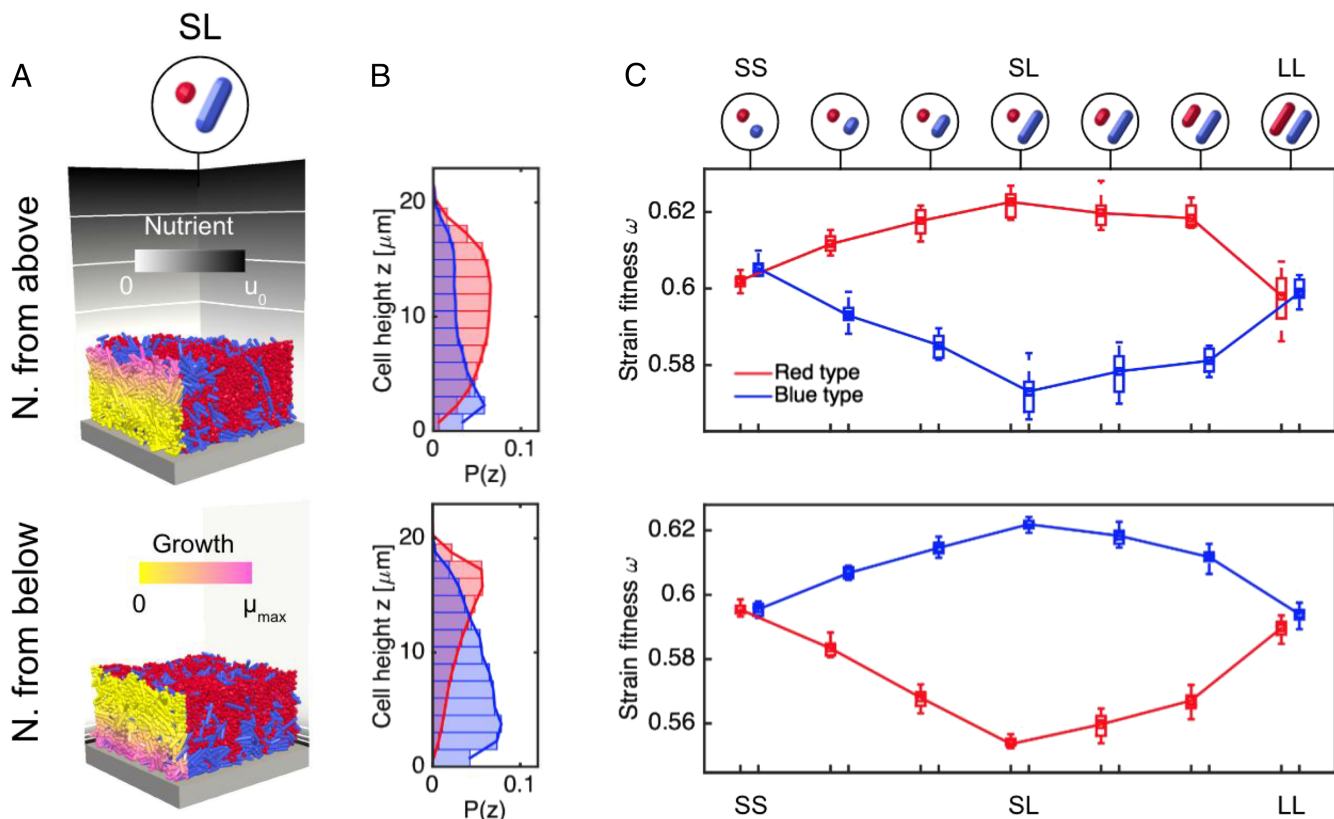
Fig. 3. Cell morphology influences strain fitness within colonies. (*A*) Competition between different cell shapes is simulated by growing biofilm sections under nutrient-limited conditions. Nutrients are supplied either from above the colony (first row) or from below (second row). Cells on the left side of the colony are colored by their growth rate, showing that rapid cellular growth is limited to a thin layer at the top or at the base of the colony, in the two scenarios, respectively. Contours on the nutrient field (background) correspond to $u/u_0 = 0.25, 0.50$ and 0.75. (*B*) Volume-weighted histograms ($P(z)$) of cell heights in nutrient-limited SL colonies show similar layering effects to those created under homogeneous growth conditions, with S cells (red) growing atop L cells (blue). (*C*) Bar plots of strain fitness show that coccal morphologies outcompete rod-like morphologies in scenarios where nutrients are delivered from above the colony, but the reverse is true when nutrients are delivered from below. There were 10 simulations per case.

vertical strain distributions seen in SS and LL control colonies are identical, confirming the absence of layering. This effect can be reproduced in 3D simulations, where cell centers and axes are not confined to the xz plane (Fig. 2 *B* and *C*).

In *SI Appendix*, we discuss further simulations carried out to interrogate the mechanism of the layering effect (*SI Appendix*, Figs. S1–S7 and Movie S2). We hypothesize that layering occurs because groups of rod-shaped cells form wedge-like structures, which, guided by the basal surface, collectively burrow beneath groups of coccal cells. The necessary group structure is, in turn, produced by steric interactions between neighboring cells and the basal surface, which produce nematic ordering in rod-shaped cells but not in coccal cells.

We also report tests that verify that the layering effect is robust with respect to changes in simulation boundary conditions (*SI Appendix*, Fig. S9), relative cell size (*SI Appendix*, Fig. S7A), simulation parameters such as the rate of division noise injection (*SI Appendix*, Fig. S7B), and changes in initial cell alignment (*SI Appendix*, Fig. S7B). However, we find that layering is completely dependent on the presence of the basal surface, confirming its importance in the layering mechanism (*SI Appendix*, Fig. S7B).

Overall, these observations suggest that individual cell shape is capable of driving significant structural changes in the wider biofilm environment—and, in particular, that combinations of differently shaped cells can drive the formation of layered structures, as reported previously in multispecies biofilms (36–38).

Shape-Driven Layering Alters Strain Fitness. Next, we examined the consequences of layering phenomena on strain competition within the biofilm environment. Because biofilms are typically characterized as highly heterogeneous environments, systematic differences in the positioning of bacterial strains could lead to significant differences in their fitness, offering a competitive advantage to particular cell morphotypes (39–41).

To examine this hypothesis, we repeated our 2D and 3D biofilm growth simulations under nutrient-limited conditions. Instead of allowing all cells to grow at the same rate as before, we coupled each cell's growth rate μ_i to the local concentration u of a rate-limiting nutrient field, evaluated at that cell's centroid $\mathbf{p}_i$. As in previous studies (26, 28, 42, 43), we model this coupling using the Monod equation $\mu_i = \mu_{max} u(\mathbf{p}_i)/(K + u(\mathbf{p}_i))$, where μ_{max} and K are the maximum specific cell growth rate and the uptake saturation constant, respectively. By imposing different boundary conditions on the nutrient reaction-diffusion equation, we created opposing perfusion scenarios: one in which nutrient was supplied from above the colony and another in which supply came from below. In each simulation, we measured the fitness of each strain, ω_{strain}, by computing the number of division events per unit time, $\omega_{strain} = \log_2(V_{strain}(t_{end})/V_{strain}(0))/t_{end}$. Here, $V_{strain}(t_{end})$ refers to the total cell volume of a strain at the endpoint of the simulation t_{end}. The results of these simulations are shown in Fig. 3. Nutrient field parameters are listed in *SI Appendix*, Table S3; these are chosen so as to create thin growth layers of similar thicknesses in the two perfusion scenarios. In both cases, the Damköhler number D (the ratio of

nutrient uptake rate to diffusion rate; *Materials and Methods*) was set to 0.01.

Fig. 3*A* provides example snapshots of both simulation scenarios, showing colonies grown from 1:1 SL cell mixtures after 12 h of growth. Cells in the bulk are colored by type as before, but cells on the left face of the colony are colored by their growth rate, indicating that rapid cellular growth is limited to a thin layer at the top or at the base of the colony, in the two scenarios respectively. In Fig. 3*B*, we plot histograms of cell heights in these colonies, showing that S and L cell strains still adopt a layered structure when grown together under nutrient-limited conditions. In *SI Appendix*, Fig. S8, we provide corresponding images and histograms for SS and LL mixtures, prepared in the same way.

In Fig. 3*C*, we explore the relationship between cell shape and strain fitness in the two nutrient competition scenarios. Here, we grow colonies not only of SS, SL, and LL cell strain mixtures but also using mixtures of intermediate cell aspect ratios. The top row of Fig. 3*B* provides a pictorial representation of the cell shapes used. Between the SS and SL cases, the birth aspect ratio of the blue strain is increased through the values 1.1, 1.5, 2.0, and 3.0. Correspondingly, the fitness of S cells increases at the expense of L cells, up to a maximum at the SL case. Next, between the SL and LL cases, the aspect ratio of the red strain is increased in the same way, and the fitness differential is reduced to ~0. When the nutrient conditions are reversed, so too is the strain fitness, this time in favor of L cells.

Importantly, our simulations confirm the hypothesis that strain layering effects can, under idealized conditions, translate into differences in strain fitness. When nutrients are delivered from above the colony, S cells receive preferential nutrient access at the expense of L cells below. S cells are correspondingly afforded an increased growth rate and gain a fitness boost relative to the SS and LL cases where no layering exists. As a result, the number of S cells present in the upper layer of the colony is enhanced, as shown by the cell height histograms in Fig. 3*B*. In cases where nutrients are delivered from below the colony, the fates of S and L cells in SL mixtures are reversed.

In both cases, we examined the effects of varying the nutrient availability in *SI Appendix*, Figs. S10 and S11, demonstrating that layering occurs irrespective of nutrient availability, but that this patterning translates into fitness differences only when the nutrient supply becomes limiting. Movie S3 shows an example of a 2D colony of S and L cells, growing with limited nutrient supply from above.

Experimental Tests of Shape-Driven Patterning. Having shown that cell shape can affect community development and composition with our model, we then sought to test our predictions experimentally. Studying cell shape empirically is challenging, because differently shaped strains will typically be physiologically different as well, introducing confounding effects. However, the *E. coli* mutants recently identified and described by Monds et al. (44) provide a solution to this impasse. Strains in this library are genetically identical except for a point mutation in the gene coding for the cytoskeletal protein MreB. Critically, these mutations cause substantial and stable changes in cell aspect ratio, without significantly affecting exponential cell growth rates, which allows cells of different shapes to be cultured together in set proportions. [For example, the specific growth rate μ is 0.519 ± 0.015 h^{-1} for the ancestral (WT) strain and 0.516 ± 0.007 h^{-1} for the mutant REL606*mreB* A53T (44).]

To test the predictions of our model in vitro, we labeled the strains with fluorescent proteins and grew bacterial colonies using binary combinations of three different *E. coli* strains: the WT REL606 strain (referred to here as WT) and mutant strains REL606*mreB* A53S (AS) and REL606*mreB* A53K (AK). Cells of these three strains exhibit mean aspect ratios of 4.44, 3.55, and 2.50 respectively (44); Fig. 4, *Inset* shows individual cells of each

these strains for visual comparison. Colonies were grown using each possible pairing of these three strains, labeled with red fluorescent protein (RFP) or GFP markers, before being imaged using epifluorescence and confocal laser scanning microscopy. The images shown are in pseudocolor, with the fluorescence signal from GFP-labeled cells shown in blue. Further details are provided in *Materials and Methods*.

Cell Morphology Drives Patterning in *E. coli* Colonies. The *E. coli* colonies reproduced several key predictions of our model. Firstly, colonies composed of only one morphotype (AK-AK, AS-AS, WT-WT) showed that degree of interstrain (red-blue) mixing is strongly dependent on cell aspect ratio. Fig. 4 shows epifluorescent images of complete colonies (top row) and confocal images of colony edge sections (bottom row). Similarly to Fig. 2 (SS column), AK-AK colonies show smooth interstrain boundaries, whereas WT-WT mixtures reproduce the fractal-like interdigitations seen in the model (Fig. 2, LL column), again recapitulating the findings of previous studies (24). The intermediate AS cell shape (Fig. 4, center column) produces an intermediate level of mixing, generating fractal-like patterns as in the WT case, but with a lower fractal dimension. In *SI Appendix*, Fig. S12, we show additional colony images for other shape combinations, demonstrating that cell shape can affect the composition of the colony edge.

Our experiments also verify that mixing long and short cell strains together can result in the emergence of layered structures, with shorter cells lying on top of longer cells. In Fig. 5*A*, we show that WT cells (shown in blue) displace shorter AK cells (red) from the base of the colony. This effect is visible both from side projections of confocal z-stacks (Fig. 5*A*, top row) and from horizontal slices taken at increasing depths in the colony. Because nutrients are supplied from the agar below the colony, we also see an overgrowth of rod cells at the colony base, as predicted by the second modeling scenario shown in Fig. 3. Reversing the color labels produces the same result (Fig. 5*B*), demonstrating that layering is not an artifact produced by the fluorescent labeling scheme.
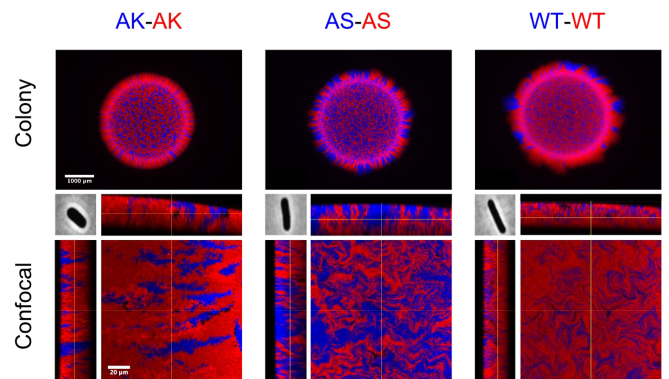
Fig. 4. Fluorescently labeled *E. coli* strains with different cell morphologies are grown together in solid culture, as an experimental test of morphotype-patterning relationships. The top row compares colonies composed of WT *E. coli* with those of actin homolog mutants *mreB*^A53S (AS) and *mreB*^A53K (AK), which differ in cell aspect ratio (*Center Inset*) but grow at the same rate. At higher magnification, representative confocal images of edge sections of each colony are shown alongside orthogonal projections (bottom row). These images corroborate the predictions of our simulations: WT colonies show complex, fractal-like mixing between red and blue cell groups, whereas AK colonies show smoother group boundaries extending vertically through the colony. AS colonies display intermediate behavior, showing patterning of lower fractal dimension than in WT colonies. Images were taken after 48 h of growth in each case. (Scale bars: top row, 1 mm; bottom row, 20 μm.) Phase-contrast cell images (of width 3.5 μm) were taken with permission from ref. 44.
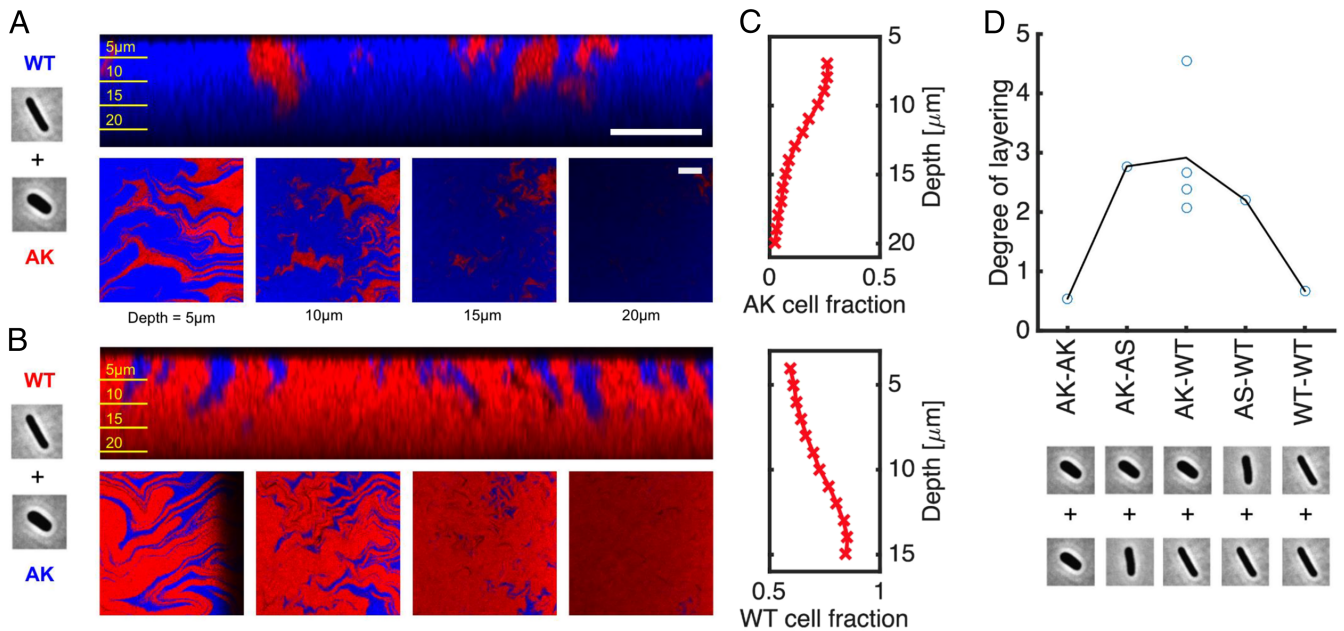
Fig. 5. Mixed-morphotype colonies reproduce the layering phenomena predicted by simulations. (*A*) Pseudocolor confocal images show that GFP-labeled WT *E. coli* (shown in blue) are able to burrow beneath shorter, wider AK mutants (red), leading to the WT cells' enrichment at the base of the colony. (*B*) The same is true when fluorescent labels are reversed. Images correspond to vertical colony sections (*A* and *B*, top row) and horizontal slices taken at successive depths (*A* and *B*, bottom row). (*C*) We quantify layering effects by measuring the volume fraction of GFP-labeled cells as a function of depth in the colony, using automated image segmentation (*Materials and Methods*). (*D*) The gradients of these traces, corresponding to the percentage gain (or loss) of GFP signal per unit depth, are compared for various binary shape combinations. Cell micrographs in *A*, *B*, and *D* are taken with permission from ref. 44. (Scale bars: 20 μm.) Confocal images and data taken after 48 h of growth.

In Fig. 5*C*, we use automated image analysis to quantify the layering effect. By counting the number of blue pixels in each layer of the stack (*Materials and Methods*), we estimate the volume fraction of AK (top row) or WT (bottom row) cells as a function of depth in the colony. These traces show an approximately linear reduction in the AK cell fraction (and corresponding increase in WT fraction) within the first 15 μm below the colony surface, which is in agreement with the cell arrangements predicted in Figs. 2 and 3.

Finally, we repeated this analysis with images taken from colonies of other morphotype combinations, including the control colonies shown in Fig. 4. In each case, we quantified interstrain layering using the average slope of the GFP fraction traces, such as those shown in Fig. 5*C*, using linear fitting. Example image segmentations, along with the complete set of GFP fraction traces, are provided in *SI Appendix*, Fig. S13. The degree of layering for each type of mixture is shown in Fig. 5*D*. As predicted by the model, we observe a strong relationship between differences in cell shape and the degree of layering in the colony across these different genotypes. Our experiments, therefore, support multiple predictions of our model (Figs. 4 and 5). Moreover, this support came without needing to tune conditions; we performed the experimental tests after the modeling. This observation suggests that the effects we report in this study are robust to experimental conditions and may be common to many existing experimental systems that use mixtures of different cell shapes.

Discussion

We have used simulations and experiments to show that cell shape can be a determinant of both spatial patterning and composition within a microbial community. In particular, we find that mixtures of rod-shaped and coccal cells can produce layered colony structures, as observed previously in both biotic and abiotic environments (36, 45). This result extends our understanding of the functional value of cell shape, both as a competitive phenotype in the biofilm context and as a means for bacteria to influence their environment through collective action.

From an evolutionary perspective, our work suggests that the biofilm environment may select for particular cell shapes in specific environments because of the ways in which they collectively influence biofilm architecture. Given the predominance of the biofilm environment for microbial life (18, 19), any selective effect produced might be expected to have a strong impact on the evolution of bacterial morphology. In natural biofilms, rapid cell growth is often limited to the upper regions of a biofilm (28, 41), which will select for coccal morphologies. Indeed, this selective pressure provides a rationale for morphological transitions associated with biofilm development (46–48) and may partly explain the ubiquity of the coccal morphology despite disadvantages, such as decreased nutrient absorption area (7).

In reality, microbial communities are far more intricate than the description used in our simulations. Like all models, our framework makes simplifying assumptions: we deliberately neglect the role of cell motility, detachment, and shear forces from the liquid surrounding the colony (42, 43, 49). Our representation of EPS secretions—a hallmark of microbial biofilms—is purely implicit, whereas the inclusion of explicit EPS particles has been shown to influence colony structure in previous studies (25, 41). Our model also neglects adhesive interactions, which could inhibit the layering effect if coccal cells were irreversibly attached to the basal surface.

However, these omissions allow a degree of realism to be traded for additional control and tractability. Rather than attempting to reproduce the exact dynamics of colony growth, our simulations instead predict the rich dynamics that can emerge when nonspherical cell shapes are introduced to existing modeling paradigms (28, 50). The fact that these predictions are corroborated by our experiments demonstrates the usefulness of this approach.

Our predictions highlight the need for further empirical and theoretical studies to examine mixed-shape colonies in more detail, treating cell shape as a physical variable instead of an incidental attribute. Bacterial strains such as those developed by Monds et al. (44) will be instrumental to this process, because they allow cellular shape to be varied in isolation of other confounding variables. Likewise, investigating how the predictions of previous theoretical studies are altered by the inclusion of morphological variability will help fully characterize the influences of cell shape in microbial communities. More generally, our work may also suggest new roles for shape and growth anisotropy in other biological systems—ultimately, shape may prove to be an important physical parameter not just for collectives of microbes but also for the morphogenesis of developing tissues and cancer tumors (51, 52).

Finally, although our study considers only antagonistic interactions between microbes, the patterning mechanisms we discuss could also influence more cooperative relationships. Metabolic exchanges between species are often associated with a layered structure in biofilms (36–38, 53–55), which suggests that shape-mediated self-organization could be used by experimenters to promote desirable colony structures. Furthermore, our results show that cell shape can affect the degree of strain mixing within the colony, which could in turn be used to control selective pressures for or against certain social strategies. For instance, because mixtures of coccal cells produce less genetic mixing than mixtures of rod-shaped cells, cooperative strategies such as enzyme secretion may become more evolutionarily stable (28). Our findings could therefore help to engineer more productive or stable synthetic microbial consortia, by selecting for community architectures that affect the interactions between strains and species (14).

Conclusions

Microorganisms of different shapes commonly grow together in their dense and genetically diverse communities, known as biofilms. We have used modeling and experiments to study the impact of cell morphology on biofilm architecture and competition. By building a simulation framework incorporating different cell shapes, we have predicted, described, and examined mechanisms of self-organization and spatial patterning driven by microbial morphology. We have also documented the same patterns emerging in real bacterial colonies. Our work suggests that cell shape is a major neglected determinant of patterning and evolutionary fitness within microbial communities.

Materials and Methods

IbM Simulations. Simulations were performed using 2D and 3D domains. In both cases, domains were surrounded by hard walls to approximate repulsive mechanical forces from the basal surface and surrounding sections of the biofilm. In *SI Appendix*, Fig. S9, we show that the hard boundary approximation reproduces the effects of periodic boundary conditions, which are more realistic but computationally more demanding. In 2D simulations, the centroids and axes of 3D capsules were confined to a plane of base length $L_x = 300$ μm, whereas 3D simulations used a cuboidal domain with base dimensions $L_x = L_y = 40$ μm. Simulations were initialized using an inoculum of cells arranged randomly on the base of the domain, with cell axis vectors drawn randomly in the 3D case. Each inoculum consisted of a 1:1 mixture of two bacterial strains, marked with red and blue color labels for lineage tracking.

In total, ≈3,000 model simulations were performed on two NVIDIA Tesla C2075 6GB GDDR5 PCIe workstation graphics cards for simulations without nutrient fields and on two NVIDIA Quadro K5000 4GB GFX graphics card for simulations including them. To account for the stochastic noise terms in our model (*SI Appendix*), we increased simulation sample sizes until our measurements converged, using the convergence criterion

$$||\langle \mathbf{X} \rangle_N - \langle \mathbf{X} \rangle_{N-1}||_{l2} \, / \, ||\langle \mathbf{X} \rangle_N||_{l2} < \epsilon_{TOL}, \qquad [1]$$

where $\langle \mathbf{X} \rangle_N$ denotes a mean vector of measurements for a sample size N, and ϵ_{TOL} is a convergence tolerance set to 5%; $||\cdot||_{l2}$ represents the Euclidean norm operation.

Simulations were visualized and checked using Paraview 4.3.1, and the postprocessing of results was carried out using Matlab 2015a. Further details on the IbM framework, including model equations and assumptions, are provided in *SI Appendix*.

Bacterial Strains and Plasmids. *E. coli* REL606 is the parent (WT) strain (56), referred to here as A53. A53K (REL606$mreB^{A53K}$) and A53S (REL606$mreB^{A53S}$) were previously constructed from REL606 with the respective nonsynonymous mutation at the 53rd amino acid residue of the MreB protein (44). A53K exhibits the shortest and widest cellular morphology, and A53S is intermediate, compared with A53. Importantly, all three strains share the same specific growth rate and differ only marginally in lag phase time (44).

We introduced plasmids pmaxRFP or pmaxGFP (Amaxa/Lonza) into all three strains for epifluorescence and confocal microscopy. For routine culturing in liquid, cells were grown shaking at 250 rpm in LB (Thermo-Fisher Scientific) at 37 °C. For plate cultures, cells were grown on Davis minimal (DM) medium (57), supplemented with 15 g · L^{-1} agar and either glucose (175 μg · mL^{-1}) or lactose (210 μg · mL^{-1}) as previously described (44) at 37 °C. All media were supplemented with kanamycin at 50 μg · mL^{-1} to maintain plasmids.

Overnight cultures were serially diluted in PBS, mixed together in a 1:1 ratio, and then spotted in either 1- or 10-μL volumes on the surface of DM plates. We observed no significant difference between glucose or lactose supplementation; data reported in this study are from glucose-supplemented plates spotted at 1-μL volume. For each combination of cell strains and fluorescent labels, control experiments using reverse labeling were also carried out. Two days following inoculation, mixed-culture colonies were imaged by epifluorescence and confocal laser scanning microscopy as previously described (41, 57).

Confocal Image Analysis. Following collection, confocal image stacks were enhanced in FIJI by setting pixel saturation to 1% and by normalizing signal to the full intensity range. Images were then segmented using the Matlab bioformats plugin, according to the following procedure. For each stack, incomplete or excessively dark images were excluded by removing any layer in which more than 1% of pixels had intensities less than 12% of the maximum, measured in composite grayscale images created by combining red and green channel data. These thresholds were chosen manually to optimize the segmentation accuracy. To ensure a sufficient number data points for curve fitting later on, confocal stacks with fewer than six images remaining were removed from the analysis outright. In each of the remaining images, the number of GFP-labeled cells was estimated by counting the number of pixels in the green channel data with intensities above a threshold, computed for each individual layer using Otsu's method (58).

1. Starr MP, Skerman VBD (1965) Bacterial diversity: The natural history of selected morphologically unusual bacteria. *Annu Rev Microbiol* 19:407–454.
2. Vos P, et al. (2011) Bergey's Manual of Systematic Bacteriology: The Firmicutes (Springer Science & Business Media, Dordrecht, The Netherlands), Vol 3.
3. Cabeen MT, Jacobs-Wagner C (2005) Bacterial cell shape. *Nat Rev Microbiol* 3(8):601–610.
4. Siefert JL, Fox GE (1998) Phylogenetic mapping of bacterial morphology. *Microbiology* 144 (Pt 10):2803–2808.
5. Tamames J, Gonzalez-Moreno M, Mingorance J, Valencia A, Vicente M (2001) Bringing gene order into bacterial shape. *Trends Genet* 17(3):124–126.
6. Kysela DT, Randich AM, Caccamo PD, Brun YV (2016) Diversity takes shape: Understanding the mechanistic and adaptive basis of bacterial morphology. *PLoS Biol* 14(10):e1002565.

7. Young KD (2006) The selective value of bacterial shape. *Microbiol Mol Biol Rev* 70(3):660–703.
8. Justice SS, Hunstad Da, Cegelski L, Hultgren SJ (2008) Morphological plasticity as a bacterial survival strategy. *Nat Rev Microbiol* 6(2):162–168.
9. Young KD (2004) Bacterial shape. *Mol Microbiol* 49(3):571–580.
10. Young KD (2007) Bacterial morphology: Why have different shapes? *Curr Opin Microbiol* 10(6):596–600.
11. Young KD (2010) Bacterial shape: Two-dimensional questions and possibilities. *Annu Rev Microbiol* 64:223–240.
12. Nakamura S, Adachi Y, Goto T, Magariyama Y (2006) Improvement in motion efficiency of the spirochete *Brachyspira pilosicoli* in viscous environments. *Biophys J* 90(8):3019–3026.
13. McLoughlin K, Schluter J, Rakoff-Nahoum S, Smith AL, Foster KR (2016) Host selection of microbiota via differential adhesion. *Cell Host Microbe* 19(4):550–559.
14. Coyte KZ, Schluter J, Foster KR (2015) The ecology of the microbiome: Networks, competition, and stability. *Science* 350(6261):663–666.
15. Wolcott RD, Ehrlich GD (2008) Biofilms and chronic infections. *JAMA* 299(22): 2682–2684.
16. Stewart PS, Costerton JW (2001) Antibiotic resistance of bacteria in biofilms. *Lancet* 358(9276):135–138.
17. Klapper I, Dockery J (2010) Mathematical description of microbial biofilms. *SIAM Rev* 52(2):221–265.
18. Costerton JW, Lewandowski Z, Caldwell DE, Korber DR, Lappin-Scott HM (1995) Microbial biofilms. *Annu Rev Microbiol* 49:711–745.
19. Hall-Stoodley L, Costerton JW, Stoodley P (2004) Bacterial biofilms: From the natural environment to infectious diseases. *Nat Rev Microbiol* 2(2):95–108.
20. Volfson D, Cookson S, Hasty J, Tsimring LS (2008) Biomechanical ordering of dense cell populations. *Proc Natl Acad Sci USA* 105(40):15346–15351.
21. Boyer D, et al. (2011) Buckling instability in ordered bacterial colonies. *Phys Biol* 8(2):026008.
22. Cho H, et al. (2007) Self-organization in high-density bacterial colonies: Efficient crowd control. *PLoS Biol* 5(11):e302.
23. Copeland MF, Weibel DB (2009) Bacterial swarming: A model system for studying dynamic self-assembly. *Soft Matter* 5(6):1174–1187.
24. Rudge TJ, Federici F, Steiner PJ, Kan A, Haseloff J (2013) Cell polarity-driven instability generates self-organized, fractal patterning of cell layers. *ACS Synth Biol* 2(12): 705–714.
25. Ghosh P, Mondal J, Ben-Jacob E, Levine H (2015) Mechanically-driven phase separation in a growing bacterial colony. *Proc Natl Acad Sci USA* 112(17):E2166–E2173.
26. Picioreanu C, van Loosdrecht MCM, Heijnen JJ (1998) Mathematical modeling of biofilm structure with a hybrid differential-discrete cellular automaton approach. *Biotechnol Bioeng* 58(1):101–116.
27. Kreft J-U (2004) Biofilms promote altruism. *Microbiology* 150(Pt 8):2751–2760.
28. Nadell CD, Foster KR, Xavier JB (2010) Emergence of spatial structure in cell groups and the evolution of cooperation. *PLoS Comput Biol* 6(3):e1000716.
29. Schluter J, Foster KR (2012) The evolution of mutualism in gut microbiota via host epithelial selection. *PLoS Biol* 10(11):e1001424.
30. Nadell CD, et al. (2013) Cutting through the complexity of cell collectives. *Proc Biol Sci* 280(1755):20122770.
31. Estrela S, Brown SP (2013) Metabolic and demographic feedbacks shape the emergent spatial structure and function of microbial communities. *PLoS Comput Biol* 9(12):e1003398.
32. Storck T, Picioreanu C, Virdis B, Batstone DJ (2014) Variable cell morphology approach for individual-based modeling of microbial communities. *Biophys J* 106(9): 2037–2048.
33. Nakayama M, Shigemune N, Tsugukuni T, Tokuda H, Miyamoto T (2011) Difference of EGCg adhesion on cell surface between *Staphylococcus aureus* and *Escherichia coli* visualized by electron microscopy after novel indirect staining with cerium chloride. *J Microbiol Methods* 86(1):97–103.
34. Matthew J, Arduino JC (2007) *Staphylococcus aureus* SEM (image 6486). Accessed July 7, 2016.
35. Rocky Mountain Laboratories, NIAID, NIH (2006) *Escherichia coli* SEM. Accessed July 7, 2016.
36. Christensen BB, Haagensen JAJ, Heydorn AJ, Molin S (2002) Metabolic commensalism and competition in a two-species microbial consortium. *Appl Environ Microbiol* 68(5):2495–2502.
37. Hansen SK, Rainey PB, Haagensen JAJ, Molin S (2007) Evolution of species interactions in a biofilm community. *Nature* 445(7127):533–536.
38. Elias S, Banin E (2012) Multi-species biofilms: living with friendly neighbors. *FEMS Microbiol Rev* 36(5):990–1004.
39. Wimpenny J, Manz W, Szewzyk U (2000) Heterogeneity in biofilms. *FEMS Microbiol Rev* 24(5):661–671.
40. Nadell CD, Xavier JB, Foster KR (2009) The sociobiology of biofilms. *FEMS Microbiol Rev* 33(1):206–224.
41. Kim W, Racimo F, Schluter J, Levy SB, Foster KR (2014) Importance of positioning for microbial evolution. *Proc Natl Acad Sci USA* 111(16):E1639–E16347.
42. Picioreanu C, Van Loosdrecht MCM, Heijnen JJ (2000) Effect of diffusive and convective substrate transport on biofilm structure formation: a two-dimensional modeling study. *Biotechnol Bioeng* 69(5):504–515.
43. Kreft JU, Wimpenny JWT (2001) Effect of EPS on biofilm structure and function as revealed by an individual-based model of biofilm growth. *Water Sci Technol* 43(6):135–141.
44. Monds RD, et al. (2014) Systematic perturbation of cytoskeletal function reveals a linear scaling relationship between cell geometry and fitness. *Cell Rep* 9(4): 1528–1537.
45. Nava GM, Friedrichsen HJ, Stappenbeck TS (2011) Spatial organization of intestinal microbiota in the mouse ascending colon. *ISME J* 5(4):627–638.
46. Serra DO, Richter AM, Klauck G, Mika F, Hengge R (2013) Microanatomy at cellular resolution and spatial order of physiological differentiation in a bacterial biofilm. *MBio* 4(2):e00103–e00113.
47. Bergkessel M, Basta DW, Newman DK (2016) The physiology of growth arrest: Uniting molecular and environmental microbiology. *Nat Rev Microbiol* 14(9):549–562.
48. Hendrickx L, Hausner M, Wuertz S (2003) Natural genetic transformation in monoculture Acinetobacter sp. strain BD413 biofilms. *Appl Environ Microbiol* 69(3):1721–1727.
49. Picioreanu C, et al. (2007) Microbial motility involvement in biofilm structure formation - a 3D modelling study. *Water Sci Technol* 55(8-9):337–343.
50. Xavier JB, Foster KR (2007) Cooperation and conflict in microbial biofilms. *Proc Natl Acad Sci USA* 104(3):876–881.
51. Heisenberg CP, Bellaïche Y (2013) Forces in tissue morphogenesis and patterning. *Cell* 153(5):948–962.
52. Basan M, Elgeti J, Hannezo E, Rappel W-J, Levine H (2013) Alignment of cellular motility forces with tissue flow as a mechanism for efficient wound healing. *Proc Natl Acad Sci USA* 110(7):2452–2459.
53. Sekiguchi Y, Kamagata Y, Nakamura K, Ohashi A, Harada H (1999) Fluorescence in situ hybridization using 16S rRNA-targeted oligonucleotides reveals localization of methanogens and selected uncultured bacteria in mesophilic and thermophilic sludge granules. *Appl Environ Microbiol* 65(3):1280–1288.
54. Wilmes P, et al. (2009) Natural acidophilic biofilm communities reflect distinct organismal and functional organization. *ISME J* 3(2):266–270.
55. Brenner K, Arnold FH (2011) Self-organization, layered structure, and aggregation enhance persistence of a synthetic biofilm consortium. *PLoS One* 6(2):e16791.
56. Lenski RE, Rose MR, Simpson SC, Tadler SC (2016) Long-term experimental evolution in *Escherichia coli*. I. Adaptation and divergence during 2,000 generations. *Am Nat* 138(6):1315–1341.
57. Kim W, Levy SB, Foster KR (2016) Rapid radiation in bacteria leads to a division of labour. *Nat Commun* 7:10508.
58. Otsu N (1975) A threshold selection method from gray-level histograms. *Automatica* 11(285-296):23–27.
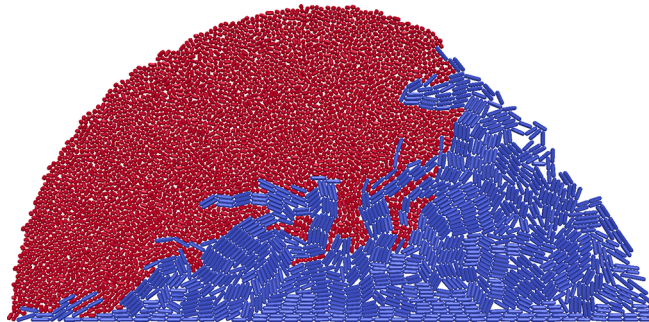
Supporting Information
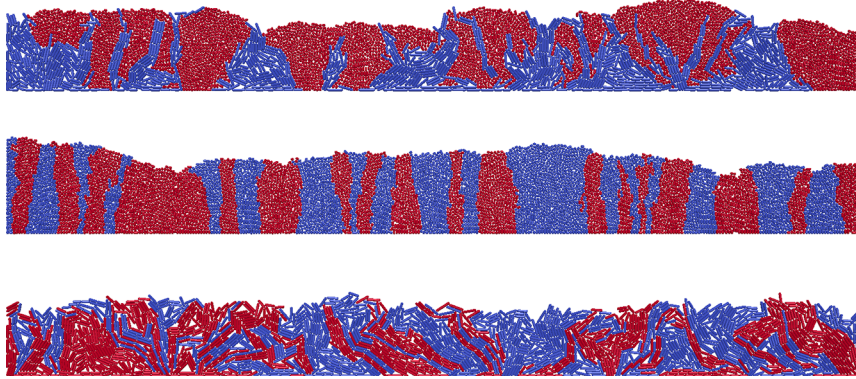
Movie S1. In this movie, we compare growing 2D colonies composed of SL, SS, and LL cell shapes (top, middle, and bottom rows, respectively), as described in Fig. 2. The movie was prepared using Paraview visualization software.

Movie S1

Movie S2. This movie shows a growing 2D colony composed of S (red) and L (blue) cell shapes, demonstrating the development of a wedge-shaped L cell group, as described in *SI Appendix*, Fig. S1. The movie was prepared using Paraview visualization software.

Movie S2
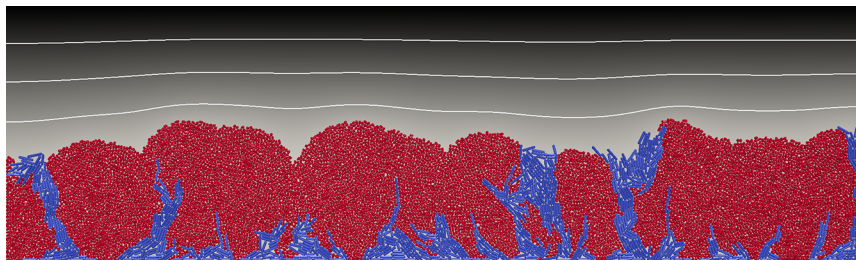
Movie S3. In this movie, we show the development of 2D colony composed of S (red) and L (blue) cell shapes, growing under limited nutrient conditions. As described in Fig. 3 and *SI Appendix*, Fig. S10, shape-driven layering leads to a growth advantage for red S cells, whose nutrient access is improved by being higher up in the colony. The movie was prepared using Paraview visualization software.

Movie S3

Other Supporting Information Files

SI Appendix (PDF)

Supporting Information

SI Text

Nematic ordering drives layering. To investigate the mechanism of cell layering in SL shape mixtures, we grew 2-D colonies from an inoculum of two cells placed a fixed distance apart. We also removed the lateral mechanical walls at $x = 0, L_x$ to exclude any influence on nematic alignment, so that colony expansion would be restricted only by the basal surface. Simulations using this simplified setup suggest that layering is driven by several interacting processes, summarized in Figure S1.
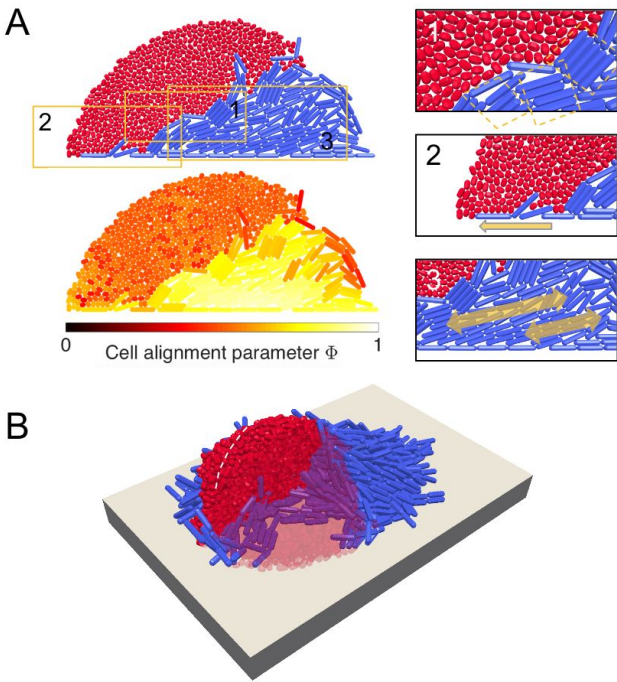
Fig. S1. Layering in SL mixtures is driven by the formation of wedge-like arrangements of L cells, which force S cells upward. A: 2-D simulations show that wedges result from steric interactions between cells, which produce high levels of cell-cell and cell-plane alignment in L cells, but not S cells. The tendency for L cells to align together has several effects that are absent in S cell groups, viz: rod cells align in cohesive, staggered files (Box 1), which are more robust to growth forces than unaligned spherical cells. Rods near the base of the colony (Box 2) are forced into alignment with the substrate plane, forming a narrow wedge tip at the red-blue clonal boundary. Rod cells to the right of this tip grow laterally (Box 3), driving the wedge under the red cell group. B: These effects are also reproduced in 3-D simulations. Cell growth rates are homogeneous, as in Figure 2.

In Figure S1-A we show two end-state snapshots of the same 2-D SL colony, coloring cells either by their type or by the value of a local pairwise orientational order parameter Φ, adapted from previous studies [1]. Φ_i is defined as

$$\Phi_i = \sum_{j \in J}^{J} c_{i,j} \varphi_{i,j}, \qquad [1]$$

where $\varphi_{i,j} = 1 - \frac{2}{\pi} \arccos |\hat{\mathbf{a}}_i \cdot \hat{\mathbf{a}}_j|$ measures the degree of alignment between a pair of cell orientation vectors $\hat{\mathbf{a}}_i$ and $\hat{\mathbf{a}}_j$, and $c_{i,j}$ is a Gaussian weighting factor given by $c_{i,j} = \exp\left(-\frac{|\mathbf{p}_i - \mathbf{p}_j|}{2\zeta^2}\right)$, where $\mathbf{p}_i$ and $\mathbf{p}_j$ are the respective cell positions. J refers to the set of neighboring cells within range 2ζ of the focal cell i, where $\zeta = 5\,\mu m$. The value of Φ measured at a focal cell increases when neighboring cells become aligned with that cell, reaching 1 when all neighbors are perfectly aligned.

As shown in Figure S1-A, steric interactions between neighboring cells in the red S-cell group are weak, and nematic ordering is correspondingly low. The lack of nematic ordering means that the group expands isotropically, as cells are not elongating or dividing in any particular direction. As a result, groups of S cells form smooth, symmetric heaps. By contrast, the level of nematic ordering in groups of L cells is very high, due to significant steric interactions between neighboring cells, as reported in several previous publications [1–3]. As a result, the growth of the colony is initially highly anisotropic, and the group becomes asymmetric and directional. This growth cell growth anisotropy has been reported previously in both experimental [4] and theoretical studies [5, 6].

We propose that the different group structures created by S and L cell shapes interact to produce layered biofilm architectures. The flatter, directed L cell groups form wedge-like structures that can slide underneath S cell groups, driving the latter upwards, as shown in Figure S1-A-1 and Movie S2. The basal plane is a vital component of this process: it prevents S cells from being displaced downwards, and increases the degree of nematic ordering in L cells close to the plane, redirecting L group growth into the S group. As shown in Figure S1-A-2, L cells are able to burrow beneath S cells because their orientations are templated to this plane: through nematic ordering, L-cell growth remains concertedly lateral, whereas S cells rapidly lose any co-planar orientation and are easily displaced upwards. Figure S1-A-3 shows that L cells behind the leading edge of the wedge also assist the layering process by providing an expansion force to drive the tip sideways under the S group. Similar behavior is observed in analogous 3-D simulations, as shown in Figure S1-B.

Variation of layering with cell shape differential. Further tests support this mechanistic description of colony layering. In Figures S2 and S3, we examine how layering, measured by the difference in mean heights for red and blue cells, varies in time as the colony grows, and as a function of the initial spacing between the two strains. We show that strain height differentials always develop at the point of collision between groups of differently-shaped cells, suggesting that layering is the result of interactions occurring at the group level. Figure S4 shows that the results of the simplified 2-D setup are replicated in 3-D, and Figure S5 demonstrates a smooth relationship between layering and cell shape difference.

Layering requires collective group structure. We also report variants of this experiment in which the structure of the L-

cell group is artificially disrupted by random mixing, which temporarily removes the height differential (Figure S6). After mixing, slow recovery of the height differential coincides with the reformation of group structure. If cell layering emerged from interactions between individual S and L cells, then the height differential would be expected to strongly increase following mixing, as this would greatly increase the number of individual contacts between S and L cell shapes. Instead we see the opposite effect, again supporting the hypothesis that sorting results from strain group interactions.

Robustness of layering effects. Figure S7 shows that the layering effect is robust with respect to changes in relative cell size (Figure S7-A), to simulation parameters such as the rate of division noise injection (Figure S7-B), and to changes in initial cell alignment (Figure S7-B). However, we find that layering is completely dependent on the presence of the basal plane (Figure S7-B).

Other shape mixtures. Our mechanistic description of the group interactions leading to layering can also explain our observations about patterns formed by SS and LL shape mixtures (shown in Figure 2). In SS colonies, a smooth vertical boundary is formed because cell orientations are unordered, so that growth forces are not exerted against the neighboring group in a concerted manner. By contrast, when L cell groups meet, neighboring cells groups concertedly grow into one another, leading to fractal-like interdigitations [7].

From these findings, we conclude that cell layering is an emergent patterning effect driven by interactions between differently-shaped cell groups. Our model predicts that groups of S and L cell shapes develop contrasting morphologies: collections of S cells expand evenly to form round groups, whereas L cells form more directed groups that lie flatter on surfaces.

Mechanical boundary conditions. The simulation domains shown in Figures 2 and 3 are bounded by hard walls on the bottom and sides, which represent the constraining forces imposed by the basal surface and surrounding sections of the colony. In the latter case, the hard wall assumption is expected to introduce boundary artifacts, because a) cell movement is blocked altogether rather than being simply constrained, and b) rod cells template their alignment to the vertical walls as they would to the horizontal surface.

Accordingly, we used the precaution of excluding cells close to side walls from our analyses (cells within $50\,\mu\text{m}$ of a side wall in the 2-D case, and within $2\,\mu\text{m}$ in 3D). We also repeated walled simulations using periodic boundary conditions (Figure S9), which recreate the lateral compressive forces without using hard walls. We found that layering dynamics in periodic simulations were very similar to those in Figure 2.

Further, the simulations described in Figures S1-S7 were carried out without using lateral walls, eliminating potential boundary effects. As shown in Figures S1 and S4, these simulations recreate the same patterning effects as seen in the bounded simulations in Figure 2, and produce an analogous layering effect – implying that hard boundaries do not exert a strong influence on the patterning dynamics.

SI Materials and Methods

Here we describe the physical basis for our IbM framework. The model is a hybridization of CellModeller, a high-

performance open-source bacterial physics engine [7, 8], and FEniCS, a finite element modeling library [9, 10], joined using a custom python interface. The source code for this framework is available online [11]; tables of model variables and parameters are provided in Tables S2 and S3 respectively.

Bacterial cell shapes. Together, groups of capsule cells comprise the structure of simulated colony, shown growing on a surface in Figure 1 (center). Each cell is represented by a rigid, elastic capsule, having fixed radius r, variable segment length l, position $\mathbf{p} = (p_x, p_y, p_z)^\top$, and orientation $\hat{\mathbf{a}} = (a_x, a_y, a_z)^\top$. Cells are assumed to be immotile, moving only as a result of elastic repulsion. We model extracellular polymeric substances, which behave as viscous fluids on cellular growth timescales [12], by overdamping cell motion.

The capsule representation allows cell shape to be parameterized using a single number: the aspect ratio $AR = 1 + l/2R$. S-type cells have an initial aspect ratio $AR_0 = 1.1$, increasing to a final value $AR_f = 1.7$ at division, whereas L-type cells have $AR_0 = 3.0$ and $AR_f = 5.7$. Perfectly spherical cells ($AR_0 = 1.0$) lack a principal axis, which we use to compute spatial relationships between cells. As such, we approximate spherical morphologies with "pseudo-spherical" capsules of $AR_0 = 1.1$.

Colony growth dynamics. We assume colony growth to be driven by three processes: nutrient diffusion and uptake, cell growth and division, and mechanical interactions between cells (Figure 1, 'Dynamics', steps 1, 2, and 3 respectively). To model the dynamics of these processes, we assume biomass accumulation to be the single dominant timescale, so that mechanical and chemical relaxation can be uncoupled from the growth scheme [13, 14]. This allows the state of the model to be updated in three consecutive stages for each simulation timestep:

1. Computing the nutrient field to pseudo-steady state, given the current cell configuration;

2. Growing and dividing cells, given local nutrient concentrations;

3. Computing cell movement using an energy optimization method, given a non-equilibrium cell configuration.

Here we discuss equations and parameters relating to each of these steps.

Nutrient fields. To compute the nutrient field $u = u(x, y, z)$ for a given cell configuration $[\mathbf{p}_1, \ldots, \mathbf{p}_N]$, we solve the reaction-diffusion equation (RDE)

$$D\nabla^2 u = \frac{1}{\gamma} \rho \mu_{\max} \left(\frac{u}{u + K} \right) \varphi(\mathbf{p}_1, \ldots, \mathbf{p}_N), \qquad [2]$$

in dimensionless form, in keeping with previous studies [15, 16]. Here, D, γ, ρ, $\mu_{\max}$, K and φ correspond to the nutrient diffusivity, the biomass yield per unit solute, the biomass density, the maximum specific nutrient uptake rate, the half-saturation concentration, and the local cell volume fraction, respectively. RDE solution behavior is governed by two dimensionless parameter groupings: the Damköhler number $\mathcal{D} = \rho \mu l^2 / D u_0 \gamma$, and the saturation number $\eta = K / u_0$, where u_0 represents the nutrient concentration in the bulk liquid above the colony. Solutions to the RDE are approximated with Newton's method,

implemented using the finite element library FEniCS [10]. Solutions are evaluated on custom-made meshes with a mesh parameter of h_n, and using a solver tolerance ϵ_n. To simulate different colony perfusion regimes, we ran biofilm growth simulations using two sets of boundary conditions, given in Table S1.

Cell growth and division. Each cell's volume V_i increases exponentially through elongation, from initial volume V_0, according to the equation $\dot{V}_i = \mu_i V_i$. Cell volumes are updated iteratively using the discretized form $\Delta V = \mu_i V_i \Delta t$, where Δt represents the simulation timestep and μ_i the cell growth rate. Cells divide lengthwise into two identical daughter cells once they reach volume $2V_0 + \xi_V$, where ξ_V represents uniform random noise in the cell cycle. Each daughter's axis vector $\mathbf{a}_i$ is perturbed slightly by a noise term with weight ξ_a, to represent spatial imperfections in the division process. A cell's growth rate is coupled via a Monod equation to the local concentration of the nutrient field u, evaluated at the cell's center $\mathbf{p}_i$, so that $\mu_i = \mu_{\max} u(\mathbf{p}_i)/(K + u(\mathbf{p}_i))$. The parameters $\mu_{\max}$ and K have the same value for all cells, so that any two cells experiencing the same nutrient concentration grow at the same rate independent of their shape.

Cell movement. Following the cell growth phase, the cell configuration is returned to a quasi-stationary mechanical equilibrium using a energy minimization algorithm. Any pair of cells whose surfaces are within $0.01\,\mu\text{m}$ of each other are deemed to be overlapping, and therefore subject to mutual repulsion. Overlaps between neighboring cells are identified and summarized in a contact matrix $\mathbf{A}$ and a distance vector $\mathbf{d}$, along with a regularizing matrix $\mathbf{M}$ representing the energetic cost of cell movement. Regularization is weighted by a scalar factor α. Then, cell impulses $\mathbf{p}$ satisfying the equation

$$\left(\mathbf{A}^\top \mathbf{A} + \alpha \mathbf{M} \right) \mathbf{p} = -\mathbf{A}^\top \mathbf{d}, \qquad [3]$$

are calculated using an iterated conjugate gradients method, such that the application of the impulses moves the cells back to an equilibrium configuration whilst minimizing cell displacement, to within an absolute tolerance ϵ_c. New overlaps created by movement are resolved sequentially, adding sets of impulses together until either their application produces no additional detectable overlaps, or until the iteration count exceeds the maximum iteration number M_{iter}. This scheme is described in further detail in previous publications [7, 8].

Table S1. Nutrient field boundary conditions used in this study

Set	Boundary	Condition	Description
A	Top: $z = \max(p_z) + h$	$u = u_0$	Supply from bulk liquid
	Bottom: $z = 0$	$\nabla u \cdot \hat{\mathbf{n}} = 0$	Zero flux through base
	Left, Right: $x = 0,\ L_x$	$\nabla u \cdot \hat{\mathbf{n}} = 0$	Zero flux through walls
B	Top	$u = 0$	Removal by bulk liquid
	Bottom	$u = u_0$	Supply from base
	Left, Right	$\nabla u \cdot \hat{\mathbf{n}} = 0$	Zero flux through walls

SI Tables

Boundary conditions for nutrient field modeling are shown in Table S1. In this table, $\hat{\mathbf{n}}$ corresponds to the unit vector normal to the boundary wall in each case. The variables and parameters used in our individual-based model are listed, along with their symbols and units, in Tables S2 and S3 respectively. Note that the dimensionless Damköhler ($\mathcal{D}$) and saturation (η) numbers are actually groupings of other parameters, as described above. Parameter sources are cited where applicable.

Bibliography.

1. Volfson D, Cookson S, Hasty J, Tsimring LS (2008) Biomechanical ordering of dense cell populations. *Proc. Natl. Acad. Sci. U. S. A.* 105(40):15346–51.
2. Cho H et al. (2007) Self-organization in high-density bacterial colonies: Efficient crowd control. *PLoS Biol.* 5(11):2614–2623.
3. Boyer D et al. (2013) Buckling instability in ordered bacterial colonies. *Phys. Biol.* 487(7405):109–113.
4. Drescher K et al. (2016) Architectural transitions in <i>Vibrio cholerae</i> biofilms at single-cell resolution. *Proc. Natl. Acad. Sci.* p. 201601702.
5. Rabani A, Ariel G, Be'er A (2013) Collective motion of spherical bacteria. *PLoS One* 8(12):e83760.
6. Storck T, Picioreanu C, Virdis B, Batstone DJ (2014) Variable cell morphology approach for individual-based modeling of microbial communities. *Biophys. J.* 106(9):2037–48.
7. Rudge TJ, Federici F, Steiner PJ, Kan A, Haseloff J (2013) Cell Polarity-Driven Instability Generates Self-Organized, Fractal Patterning of Cell Layers. *ACS Synth. Biol.* 2(1):705–414.
8. Rudge TJ, Steiner PJ, Phillips A, Haseloff J (2012) Computational modeling of synthetic microbial biofilms. *ACS Synth. Biol.* 1(8):345–52.
9. Logg A, Wells GN (2010) Dolfin. *ACM Trans. Math. Softw.* 37(2):1–28.
10. Alnæs MS et al. (2015) The FEniCS Project Version 1.5. 3(100):9–23.
11. Smith WPJ (2016) Cellmodeller4 branch. [Online; accessed July 13, 2016].
12. Klapper I, Rupp CJ, Cargo R, Purvedorj B, Stoodley P (2002) Viscoelastic fluid description of bacterial biofilm material properties. *Biotechnol. Bioeng.* 80(3):289–296.
13. Picioreanu C, Van Loosdrecht MCM, Heijnen JJ (2000) Effect of diffusive and convective substrate transport on biofilm structure formation: A two-dimensional modeling study. *Biotechnol. Bioeng.* 69(5):504–515.
14. Klapper I, Dockery J (2010) Microbial Biofilms. 52(2):221–265.
15. Picioreanu C, van Loosdrecht MC, Heijnen JJ (1998) Mathematical modeling of biofilm structure with a hybrid differential-discrete cellular automaton approach. *Biotechnol. Bioeng.* 58(1):101–16.
16. Nadell CD, Foster KR, Xavier JB (2010) Emergence of spatial structure in cell groups and the evolution of cooperation. *PLoS Comput. Biol.* 6(3):1–9.

Table S2. Model variables used in this study

Variable	Symbol	Units
Cartesian coordinates	x, y, z	µm
Cell volume fraction field	ϕ	
Nutrient field	u	$\mathrm{kg\,m^{-3}}$
For each cell i		
position vector	$\mathbf{p}_i = (p_x, p_y, p_z)^\top$	µm
orientation unit vector	$\hat{\mathbf{a}}_i = (a_x, a_y, a_z)^\top$	µm
segment length	l_i	µm
volume	$V_i = \pi l_i r^2 + \frac{4}{3}\pi r^3$	µm³
local nutrient concentration	$u_i = u(\mathbf{p}_i)$	$\mathrm{kg\,m^{-3}}$
growth rate	$\mu_i = \mu_{\max} u_i / (K + u_i)$	$\mathrm{s^{-1}}$

Table S3. Model parameters used in this study

| Parameter	Symbol	Value	Units	Source
Domain size:			µm	[15]
width	L_x	300 (2D) or 40 (3D)		
depth	L_y	1 (2D) or 40 (3D)		
height	L_z	$L_z = \max(p_z) + h$		
Cell radius	r	0.48	µm	This study
Cell birth aspect ratio:	AR_0			This study
S-type		1.1		
L-type		3.0		
Boundary height	h	40	µm	[15]
Nutrient diffusivity	D	2×10^{-9}	$\mathrm{m^2\,s^{-1}}$	[15]
Bulk concentrations:	u_0		$\mathrm{g\,m^{-3}}$	This study
case 1: unlimited		∞		
case 2: rich		50		
case 3: poor		5		
Dimensionless parameters	$(\mathcal{D}, \eta)$			This study
case 1: unlimited		(0, 0)		
case 2: rich		(0.001, 0.0033)		
case 3: poor		(0.01, 0.033)		
Biomass density	ρ	290	$\mathrm{kg\,m^{-3}}$	[15]
Specific uptake rate	$\mu_{\max}$	15.2×10^{-6}	$\mathrm{s^{-1}}$	[15]
Uptake saturation constant	K	0.35×10^{-3}	$\mathrm{kg\,m^{-3}}$	[15]
Biomass yield	γ	0.045		[15]
Newton solver tolerance	ϵ_n	1×10^{-3}		This study
Mesh element size	h_n	5	µm	This study
Division axis noise	ξ_a	9	%	[8]
Division volume noise	ξ_V	0.2	%	[8]
Regularization weight	α	0.04		[8]
CG Solver tolerance (abs.)	ϵ_c	1×10^{-3}		[8]
Max. contact iterations	M_iter	8		[8]
Cell grid element size	h_c	10	µm	This study
Time step	Δt	10	min	[8]
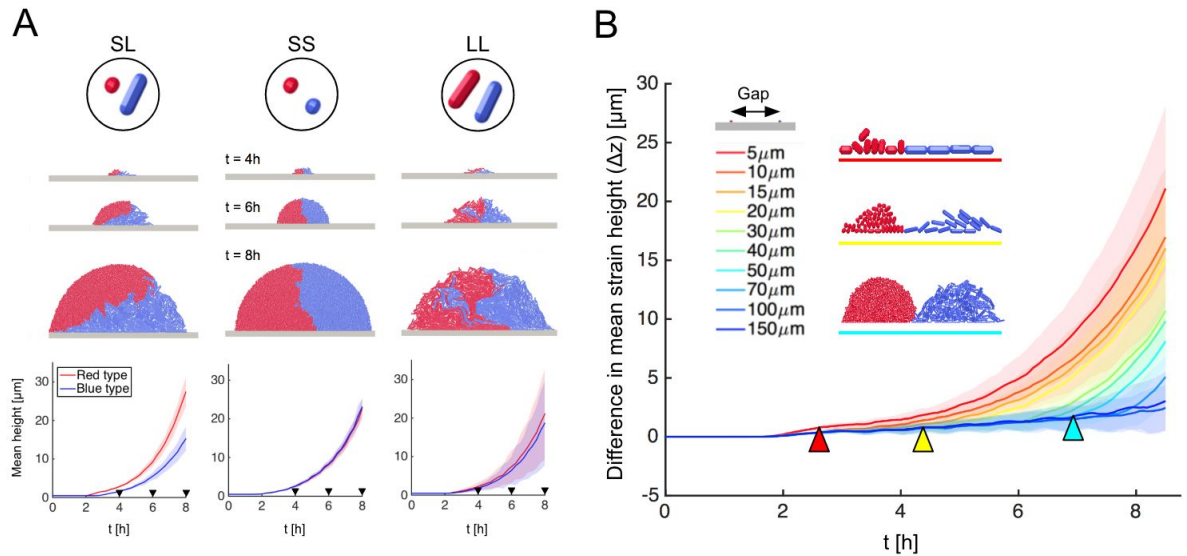
Fig. S2. Simplified 2-D simulations allow the physical mechanism of cell sorting to be explored. A: 2-group simulations using SL, SS and LL colonies form layered, smooth and interdigitated cell distributions respectively. Traces of mean cell height quantify the layering effect over time in SL colonies; black arrows indicate snapshot times. 100 simulations per case. B: Changing the initial gap between the cells alters the size of the groups at the time at which they meet. In all cases, a difference in the mean strain heights (Δz) begins to develop as soon as the groups collide, regardless of the group size. Example snapshots of colliding groups are shown for initial gaps of 5, 20 and $50\,\mu\text{m}$ (inset); collision times are marked on the graph by triangles of the corresponding color. Upon collision, the rate of splitting is increased. 20 simulations per case; cell growth rates are homogeneous.
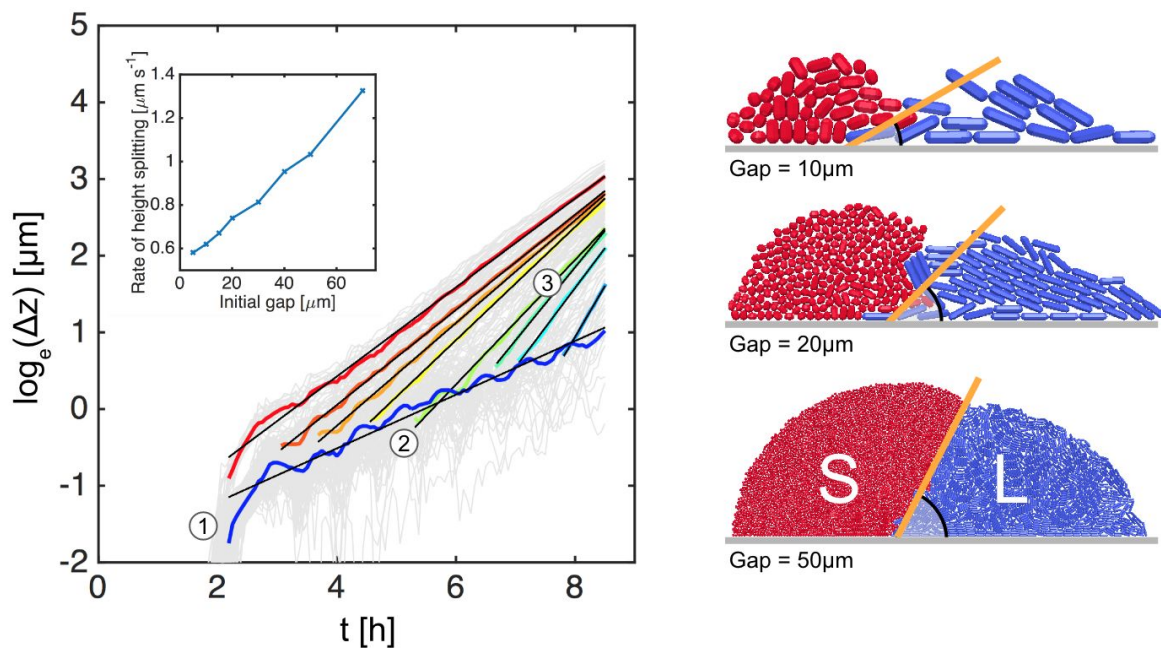
Fig. S3. Further analysis of the 2-group cell sorting experiments shown in Figure 3-B show that the cell layering rate increases with group size. Three separate process contribute to the growth of a strain height differential Δz: an initial jump (1) precedes a shallow, sustained climb (2), followed by a steeper climb as soon as the S and L cell groups collide (3). Fitting lines to these traces shows that the rate of height splitting after collision increases with initial gap (inset), suggesting that the strain sorting mechanism is dependent on group size. This observation supports the hypothesis that cell sorting is driven by group structure: increases to the initial gap change the shape of L cell groups at the point of collision, from shallow wedges (Gap = 10μm case) to steeper wedges (Gap = 50μm case). As the wedge gradient increases, so too does the rate of spitting. Trace color legend identical to that shown in Figure S2. 20 simulations per case; cell growth rates are homogeneous.
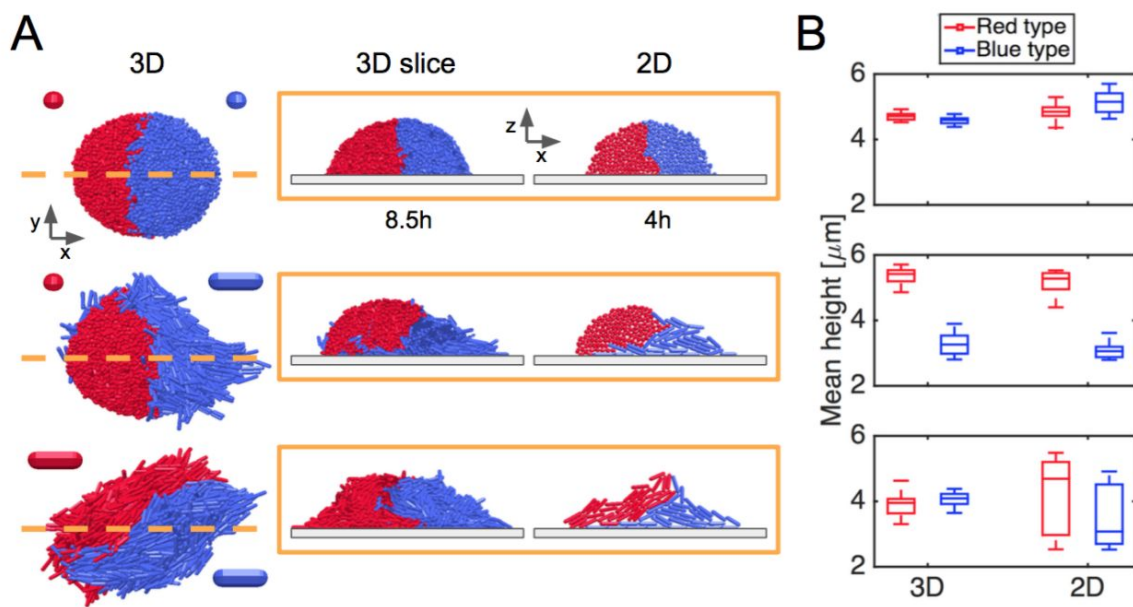
Fig. S4. Repeats of 2-group colony growth simulations in 3 dimensions reproduce the spatial patterning seen in 2-D (Figure S2-A). (A) shows overhead views of 3-D colonies (first column), grown using the SS (first row), SL (second row) and LL (third row) shape combinations. 2-D slices taken through these colonies (yellow boxes, left column) show similar colony shapes and cell strain distributions to 2-D simulations of the same overall height (yellow boxes, right column). Snapshots shown are representative in each case, and dashed lines indicate the slice plane orientation. (B) quantifies the comparison using the mean cell height metric, showing that the cell sorting effect is common to both 3-D and 2-D geometries. Data collected at same timepoints as in (A); boxes and whiskers show interquartile and absolute ranges, respectively. 20 simulations per case; initial gap of 6µm. Cell growth rates are homogeneous.
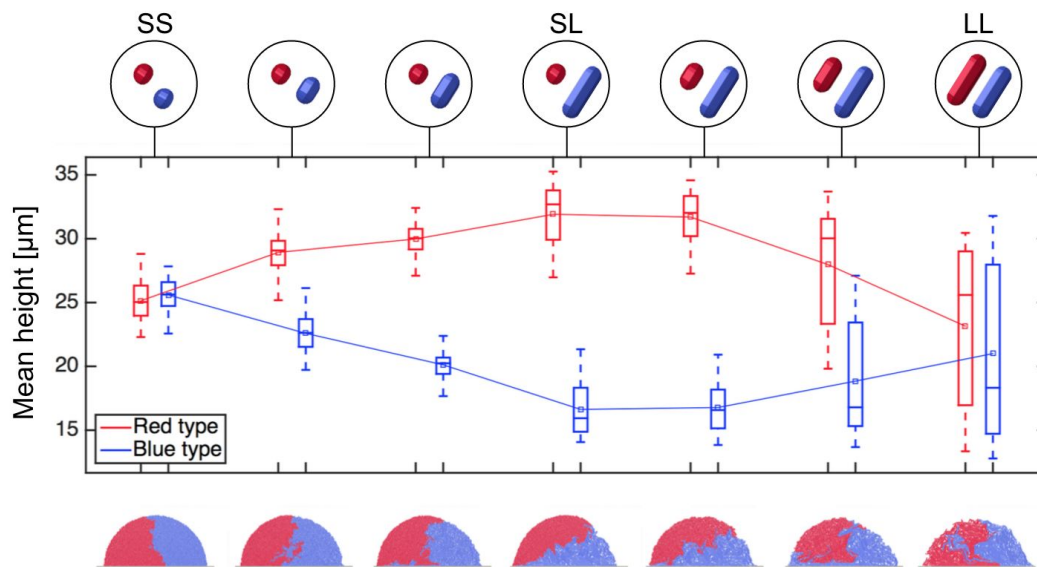

Fig. S5. Simulations using intermediate cell shapes show smooth transitions in strain height differentials between the SS, SL and LL cases discussed in Figure S2-A. As the aspect ratio of the blue strain is increased, the height differential rises (SS to SL). Then, increasing the aspect ratio of the red strain in the same way extinguishes the height differential but leads to greater height variance (SL to LL). Solid lines denote means; boxes and whiskers show interquartile and absolute ranges, respectively. Data and snapshots taken after 8h of growth in 2-group simulations. 100 repeats per case; cell growth rates are homogeneous.
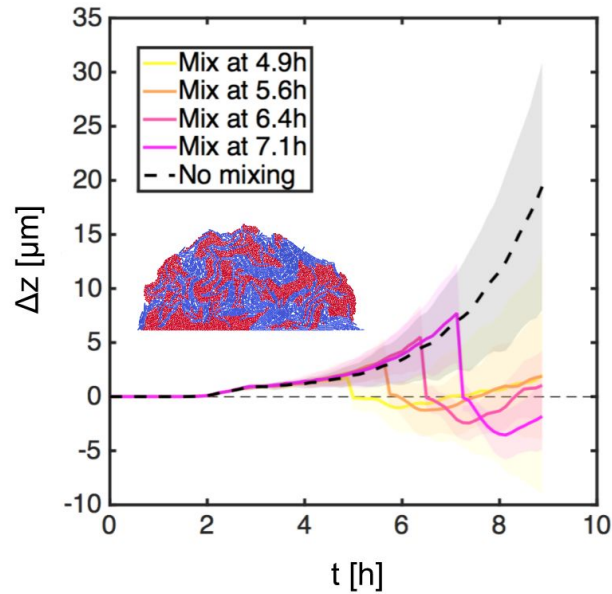
Fig. S6. The cell layering mechanism relies on group structure. Repeats of simplified 2-group simulations (Figure S1) show that the strain height differential Δz does not fully recover following random mixing events at 4.9, 5.6, 6.5 or 7.1h. At these times, strains are mixed by randomly changing each cell's strain identity with probability 0.5, so that approximately half the S strain population (red) converts to the L-type morphology (blue) and vice-versa. Shortly after mixing, the height differential begins to rise gradually as small groups of L shapes reform surface-hugging group structures, as shown in the inset colony snapshot (8h growth, following a mixing event at 4.9h). These observations can be used to exclude the possibility that strain layering emerges at the individual level - in this case, mixing events would generate more S-L contacts, resulting in a rapid recovery of the height differential. Bold lines and shaded areas correspond to mean values and 95% confidence intervals respectively. All simulations use an initial gap of 6μm. 20 simulations per case; cell growth rates are homogeneous.
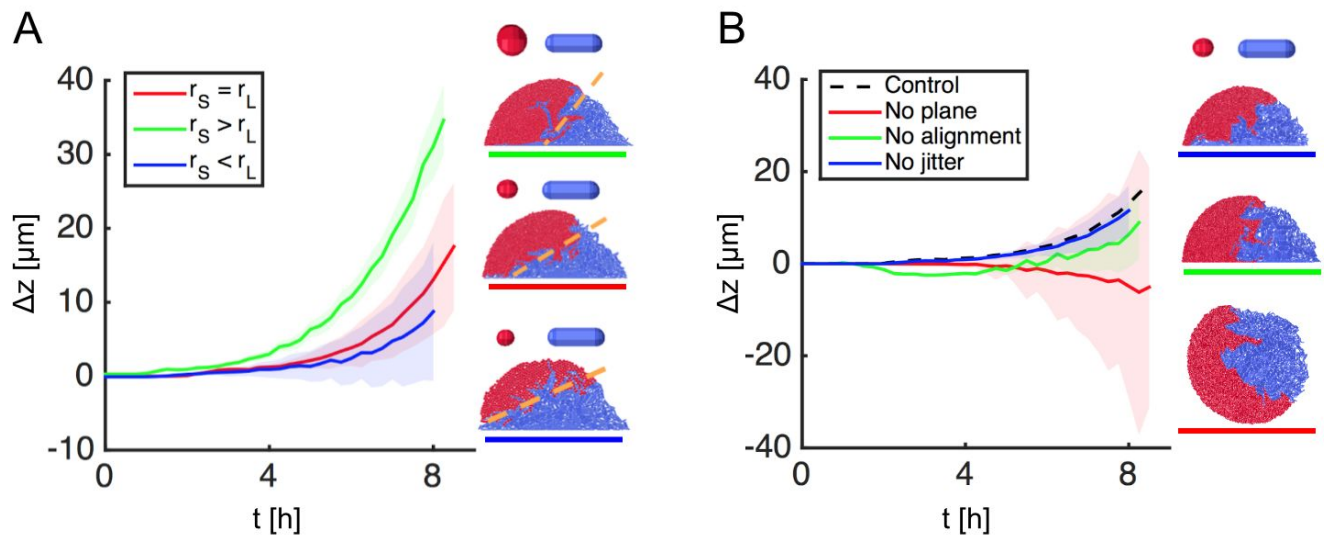

Fig. S7. Additional 2-group simulations provide further support for the layering mechanism proposed in Figure S1. (A): the layering effect, characterized by time traces of mean strain height difference Δz, has a weak dependence on relative cell size, as demonstrated with simulations using modified S-type cells of different radii but identical aspect ratios ($AR_0 = 1.1$). Smaller cells burrow more easily beneath larger ones regardless of shape, which can either attenuate sorting ($r_S > r_L$ case) or enhance it ($r_S < r_L$ case) relative to the original ($r_S = r_L$ case). (B): Sorting is robust to changes in division orientation noise (no jitter), and to initial cell orientation (no alignment), but is extinguished when the basal plane is removed. Bold lines and shaded areas correspond to mean values and 95% confidence intervals respectively. All simulations use an initial gap of 5μm. 20 simulations per case; cell growth rates are homogeneous.
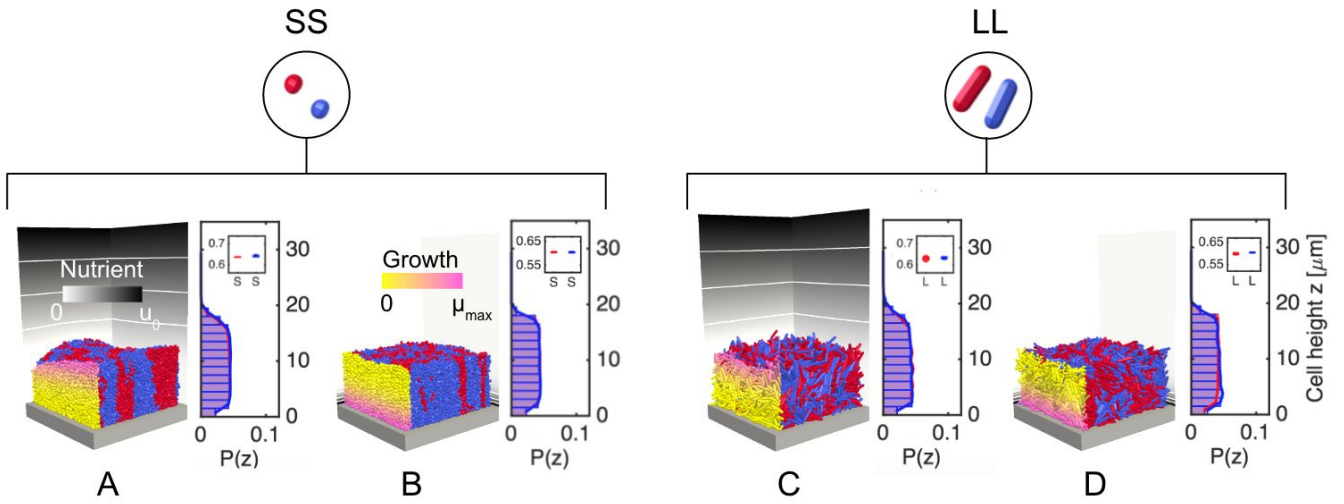
Fig. S8. Control simulations show that fitness benefits must result from the heterogeneous colony structures produced in SL mixtures. In contrast to the layering observed in SL colonies (Figure 3), vertical cell volume distributions ($P(z)$) are identical in SS and LL control simulations. Correspondingly, no fitness difference between strains is observed – regardless of whether nutrients are delivered from above the colony (A, C) or from below (B, D). Note that in both growth scenarios, strain fitnesses are the same in SS and LL colonies, highlighting that shape has no direct effect on cell growth rates in our model.
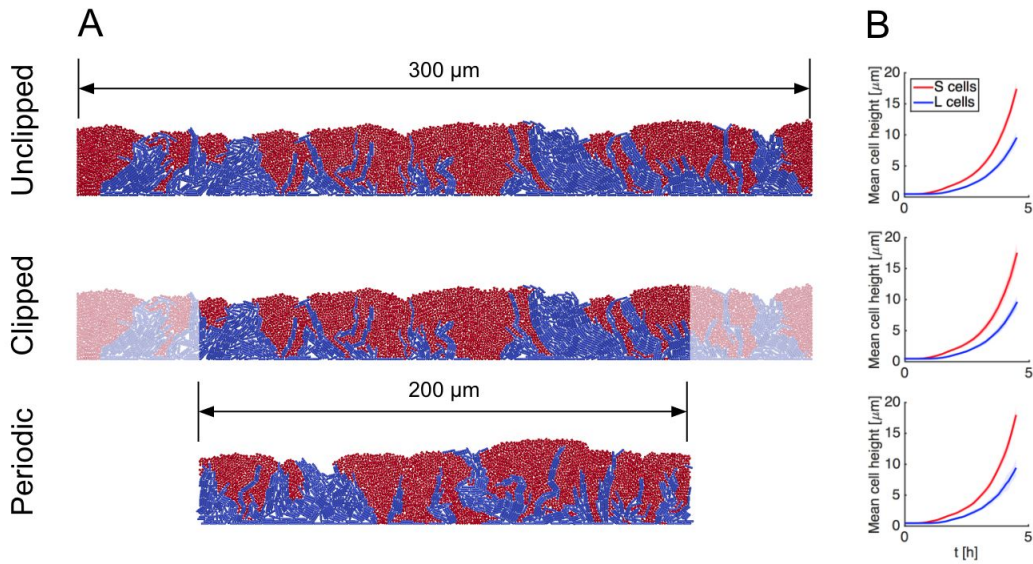

Fig. S9. Mixed-shape simulations using hard and periodic mechanical boundaries behave similarly. Here we compare 2-D simulations featuring hard lateral walls (such as those shown in Figures 2, S10 and S11), before and after excluding cells within 50μm, with periodic analogues of equivalent domain sizes. Colony snapshots (A), taken after 4.5h of growth, show unclipped, clipped and periodic simulations, which produce similar group structures. All three cases produce similar layering dynamics, as quantified by mean strain height traces (B). Sample of 5 simulations under uniform growth conditions, initiated as described in the main text; cell growth rates are homogeneous.
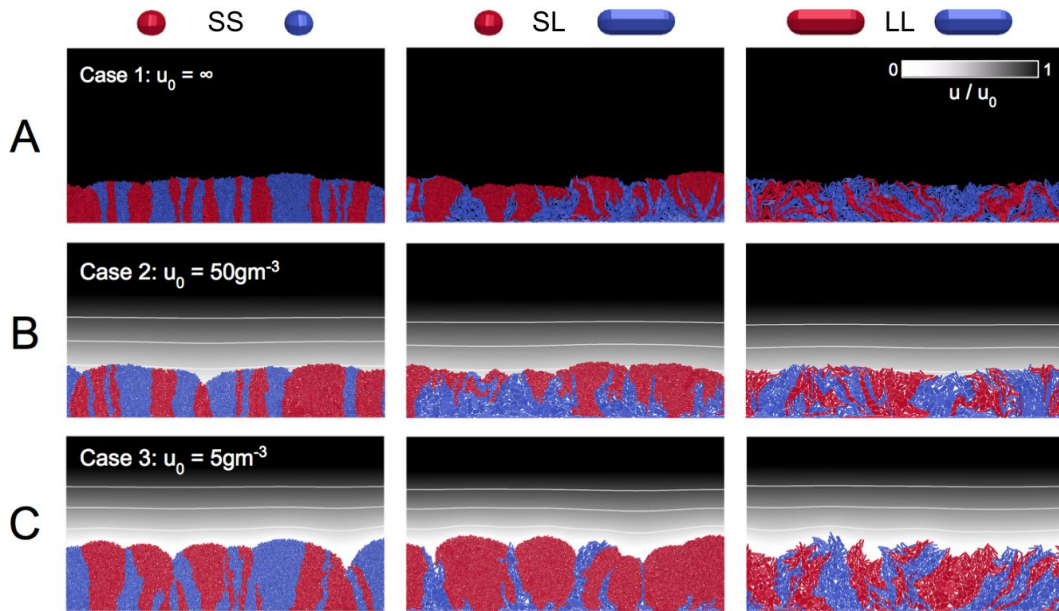
Fig. S10. 2-D Repeats of 3-D colony competition simulations (Figure 3) show that the 3 distinct modes of spatial patterning occur irrespective of nutrient availability. Colonies composed of SS (first column), SL (second column) and LL (third column) shape mixtures were grown under conditions of unlimited (Case 1, row A), rich (Case 2, row B) or poor (Case 3, row C) nutrient supply from above the colony. Damköler numbers are 0, 0.001 and 0.01 respectively. Contours indicate points where $u/u0 = 0.25, 0.50$ and 0.75. Colony snapshots in rows (A) and (B) show sorting patterns similar to those discussed in Figure 3. However, significant differences in strain growth rates appear when nutrient supply becomes limited (C), so that S cells overgrow the top of the colony.
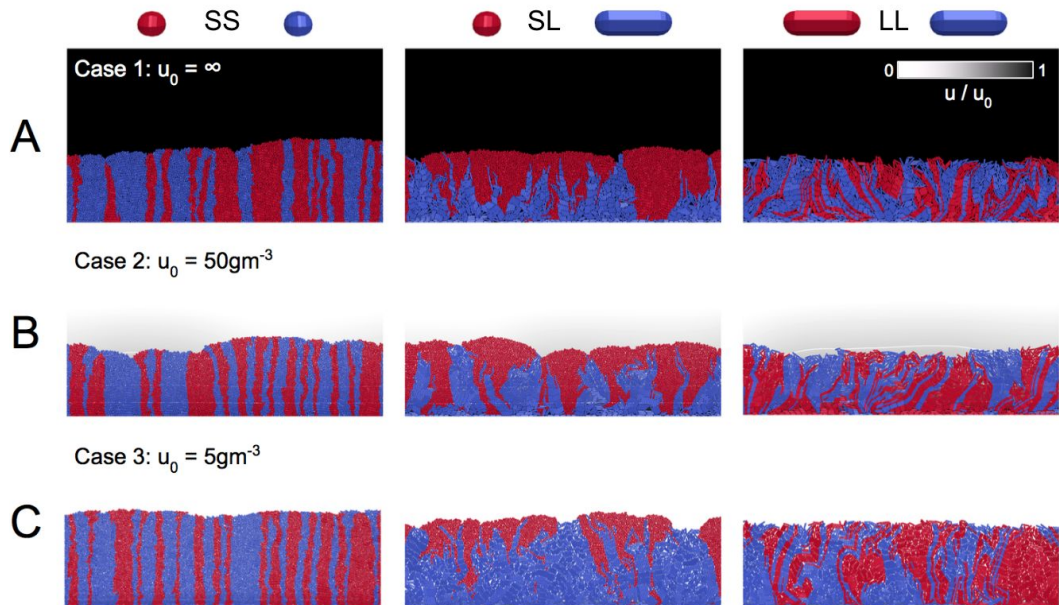
Fig. S11. 2-D colony competition simulations show that spatial patterning occurs irrespective of nutrient availability (A, unlimited; B, rich; C, poor) in simulations where nutrient is delivered from below the colony. Here we see similar behavior to Figure S10, except that now L cells receive preferential nutrient access over S cells in SL colonies, causing them to dominate the base of the colony (middle column, row C). Nutrient contours are obscured by cells. Note that in row C colony fronts are smoother since surface instability effects have been removed by the change in boundary conditions. 20 simulations carried out per case.
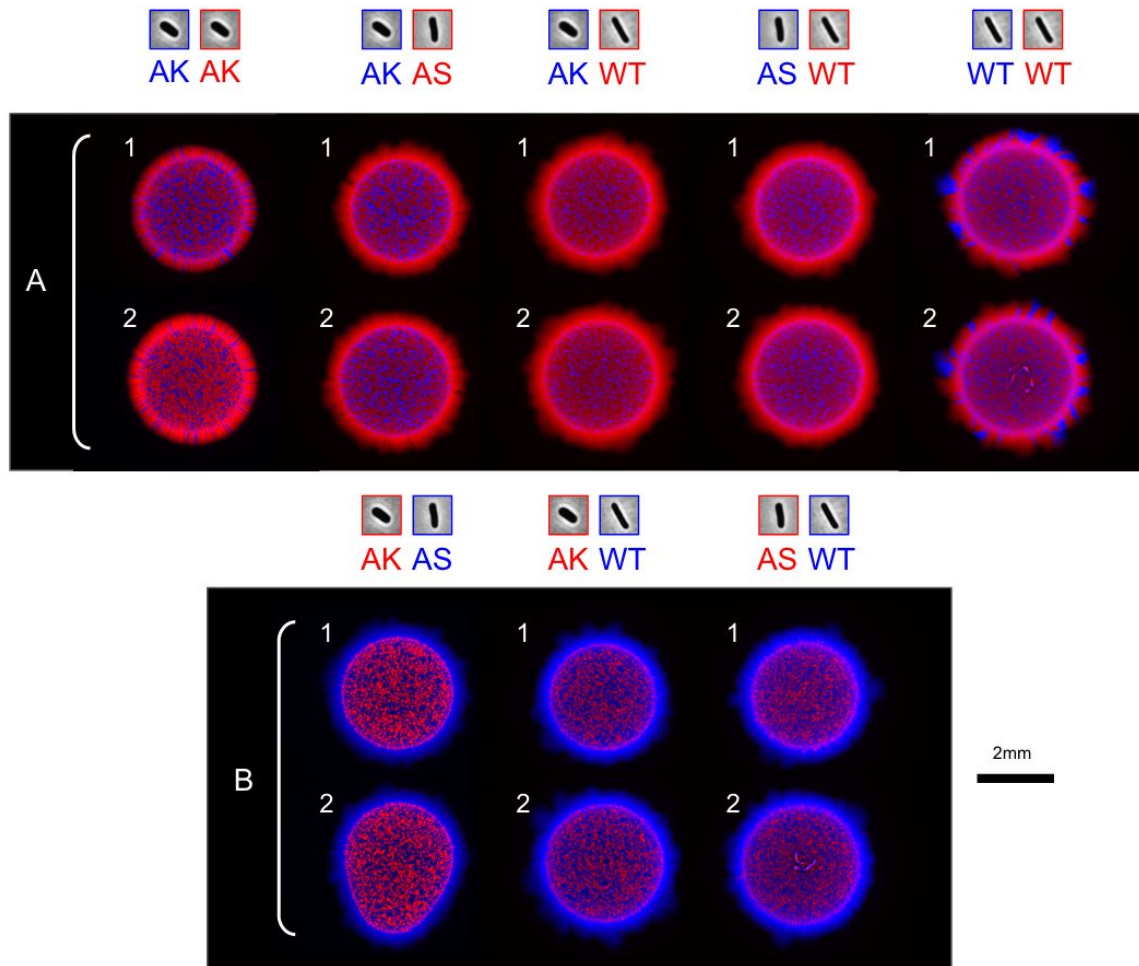
Fig. S12. Cell shape affects colony edge composition. Here we show pseudocolor images of whole *E. coli* colonies as in Figure 4, for different binary combinations of AK, AS and WT strains. In each case, two experimental replicates (1, 2) are provided. In A, strains are shown in red (longer cell strain, rfp label) and blue (shorter cell strain, gfp label). As the aspect ratio of the red strain is increased (AK-AK through AK-WT), its presence at the colony edge increases relative to the shorter blue type. Applying the same procedure to the blue strain (AK-WT through WT-WT) extinguishes the effect. This trend can be seen both in colonies containing mutant strains (AK, AS) and in those containing the ancestral strain (WT) – suggesting that the effect is not caused by mutations per se, but by the cell shape changes they produce. In B, red and blue fluorescent labels are reversed, and the same trend appears.
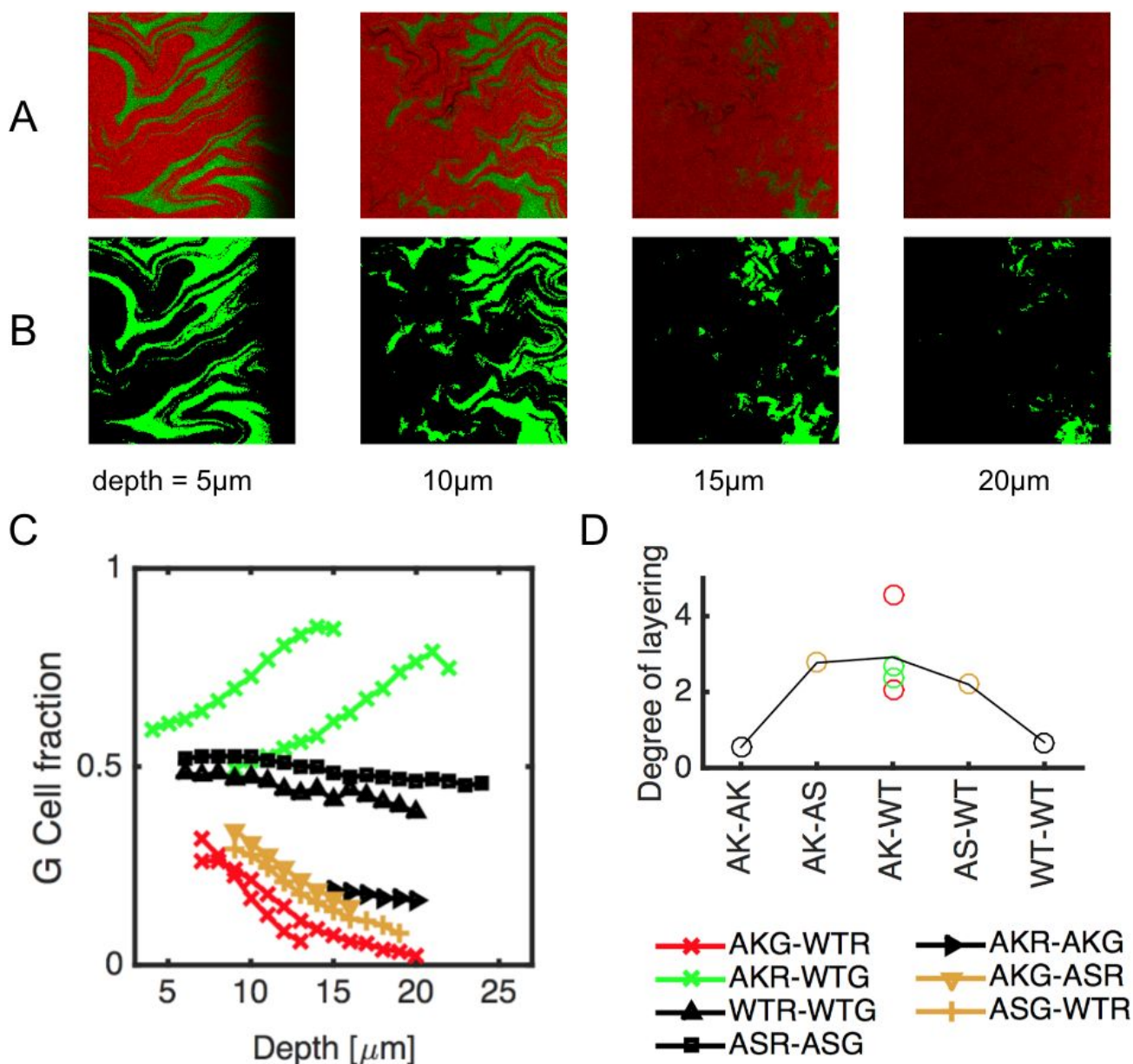
Fig. S13. Quantification of cell layering effects using image analysis. Red-green confocal image stacks (A, shown in pseudocolor in the main text) were segmented using the green channel only (Materials and methods) to produce binary images (B). In C, we plot the fraction of green pixels in these segmentations as a function of depth in the colony, for various binary cell shape mixtures. Each line corresponds to one segmented confocal stack; lines are colored red, green, black or orange to denote mixed-morphotype treatments, color-swapped treatments, single-morphotype controls and intermediate morphotype treatments respectively, as shown in the key (bottom right). The strains (AK, AS, WT) and fluorescent labels (G, R) used in each binary mixture are specified. The gradients of these traces, extracted using linear regression, are plotted in D (Replotted from Figure 5) with data points color-coded to match (A). Images and data taken after 48h growth in each case.